COMPUTATIONAL ANALYSIS OF VARIOUS REACTIONS BETWEEN HYDROXYL RADICALS AND ORGANIC MERCURY SPECIES

by

Cody James Perry, B.S.

THESIS

Presented to the Faculty of

The University of Houston-Clear Lake

In Partial Fulfillment

Of the Requirements

For the Degree

MASTER OF SCIENCE

in Chemistry

THE UNIVERSITY OF HOUSTON-CLEAR LAKE

AUGUST, 2021

COMPUTATIONAL ANALYSIS OF VARIOUS REACTIONS BETWEEN HYDROXYL RADICALS AND ORGANIC MERCURY SPECIES

by

Cody J. Perry

APPROVED BY

_____

Yi Su, Ph.D., Chair

_____

Anton Dubrovskiy, Ph.D., Co-Chair

_____

Daniel Wang, Ph.D., Committee Member

RECEIVED/APPROVED BY THE COLLEGE OF SCIENCE AND ENGINEERING:

_____

David Garrison, Ph.D., Interim Associate Dean

_____

Miguel Gonzalez, Ph.D., Dean

Dedication

To my parents, mentors, and friends who helped me get to where I am today.

Acknowledgements

I would like to start by acknowledging both my parents Marilyn and Ronald Perry, for the unending love and support through all my studies. I would not be where I am today without their incredible support. I would also like to acknowledge the Knuckleheads and their parents who always have my back.

I want to say a special thanks to both Dr. Anton Dubrovskiy and Dr. Yi Su for allowing me to do research in both of their labs concurrently and supporting me as I needed. Thanks to their guidance I have been able to learn more about myself as a researcher. I would also like to thank Dr. Su, Dr. Dubrovskiy, and Dr. Daniel Wang for helping me apply for my Ph.D. candidacy. Thanks to their support, I will be going to the University of California Riverside in the Fall of 2021.

I am grateful to have been supported by the Welch Foundation for my research. Our lab has been supported by the Pittsburgh Supercomputer Center and allowing us to use their Bridges supercomputer. I also want to thank Dr. Theodore Dibble for his support with computational chemistry and extra guidance in this project.

ABSTRACT

COMPUTATIONAL ANALYSIS OF VARIOUS REACTIONS BETWEEN HYDROXYL RADICALS AND ORGANIC MERCURY SPECIES

Cody James Perry
University of Houston-Clear Lake, 2021

Thesis Chair: Dr. Yi Su
Co-Chair: Dr. Anton Dubrovskiy

The interactions between hydroxy radicals and both dimethylmercury and methylmercury hydroxide have been studied using *ab-initio* methods. The density functional theory (DFT) method M06-2X was used to optimize the structures of the stationary points in each reaction channel. The single point energies were determined using coupled-cluster theory (CCSD(T)). For the reaction with dimethylmercury there are three possible channels, with the favored product as methylmercury hydroxide with the smallest energy barrier of 7.3 kcal mol^{-1} ($k(TST)=1.23x10^{-12}$ cm^3 $molecule^{-1}$ s^{-1}). For the reaction between hydroxyl radical and methylmercury hydroxide there are six possible channels with the most probable channel being a hydrogen abstraction to form MeHgO radical. This channel has the lowest energy barrier of 2.5 kcal mol^{-1} with a rate constant of $3.87x10^{-9}$ cm^3 $molecule^{-1}$ s^{-1}. Based on these results, dimethylmercury will undergo demethylation due to hydroxyl radicals whereas methylmercury hydroxide will not.

TABLE OF CONTENTS

LIST OF TABLES

LIST OF FIGURES

CHAPTER I:

INTRODUCTION

Mercury as a Global Contaminant

Mercury is a non-nutritive heavy metal that poses significant environmental and health concerns. With 80 electrons, mercury is the final transition metal in the 6th row of the periodic table. Mercury is an abnormal metal, possessing unusual properties for its location on the periodic table such as being a liquid at room temperature. Mercury has two main oxidation states, Hg(I) and Hg(II). These oxidized mercury compounds are some of the most dangerous forms of mercury as, unlike Hg(0), they tend to be more reactive with other species.

Mercury has a wide variety of uses in industry, medicine, dentistry, batteries, science, and military applications. Many old thermometers were used with mercury as it had constant thermal expansion. Atmospheric pressure was once measured using mercury as well, leading to the creation of millimeters of mercury (mmHg or torr).

The World Health Organization (WHO) has estimated that each year 10,000 tons of mercury is released globally from both natural and anthropogenic sources. These emissions find their way to various ecosystems causing contamination and irreparable damage. Industrial age anthropogenic mercury is estimated as 640,000 tons.[1] The burning of fossil fuels and medical waste incineration accounts for more than 80% of all anthropogenic sources.[2] The released mercury is then converted to inorganic mercury in the atmosphere. This inorganic mercury can then seep into the soil or water ways, leading to the production of organic mercury.

While all mercury species are toxic, organic mercury is the most toxic form. It is widely accepted that organic mercury can be formed biotically and abiotically by the methylation of inorganic mercury in natural environments.[3] Methylmercury is a

neurotoxin and can be bioaccumulated and magnified through the food web in natural environments. Methylmercury hydroxide specifically has a large presence in the wood web, starting from ocean plant life to the fish that are consumed by humans. Consumption of fish contaminated by methylmercury poses health risk to humans, and the WHO's guideline is 0.5ug/g for mercury level in fish. In Japan, large amounts of mercury were dumped into the water of Minamata Bay by accident, causing thousands of cases of mercury poisoning in 1956, leading to what was dubbed as Minamata disease.[4]

Dimethylmercury (DMM) is a volatile and highly toxic form of organic mercury contaminant. There are few uses of dimethylmercury left, mostly being laboratory procedures, as the risk of use far outweighs the benefits. Study into dimethylmercury focuses on its fate since dimethylmercury constitutes a significant fraction (up to 80%) of the methylated mercury pool.[5,6] It has been suggested that dimethylmercury is an important source of methylmercury in certain aquatic environments.[7] Even though DMM has been shown to be relatively stable in water[8], little is known for the reaction of DMM and with the most important reactive species, such as OH radical, which can be formed easily in oceanic conditions. I believe that such reactions are extremely important to understand the fate and impact of DMM in nature aquatic environments. The three thermodynamically accessible reaction channels present in the interaction of dimethylmercury and a hydroxyl radical will be studied:

Reaction Channel 1: $MeHgMe + \bullet OH \rightarrow MeHgOH + \bullet CH_3$

Reaction Channel 2: $MeHgMe + \bullet OH \rightarrow MeHgCH_2\bullet + H_2O$

Reaction Channel 3: $MeHgMe + \bullet OH \rightarrow MeHg\bullet + CH_3OH$

Experimental reports on reactions involving DMM are scarcely found. In 1983 Niki et al utilized FT-IR to study the interaction between DMM and OH radical and

found MeHgOH as the favored product.[9] An interesting result of this study was the lack of methanol present in the products, leading to the belief that the activation energy of this third reaction channel might be too high to occur at room temperature. To my best knowledge, this is the only present work on this interaction, leaving much be discovered.

Methylmercury Hydroxide as a Global Contaminant

Organic mercury is one of the most toxic forms of mercury with the ability to bioaccumulate in aquatic ecosystems. Most organic mercury in aquatic environments is found as compounds of $MeHg^+$ as it is highly soluble in water. The two most prominent forms of $MeHg^+$ is MeHgOH and MeHgCl. These molecules can be treated as $MeHg^+ + {}^-OH/{}^-Cl$ as the Hg-X bonds are more ionic in nature.[10] The presence of MeHgOH is well established and the production has been shown to occur in sulfur containing sediments and sulfur containing biotic species.[5,6,10] MeHgOH has been reported as the product from reactions of dimethylmercury MeHgMe such as photolysis. MeHgOH and $MeHg^+$ are believed to be the dominant species at low Cl^- concentration (<10 mg/L).[11] Tossell et al.[11] indicate that $MeHgOH_2^+$ and MeHgOH are the most important species even in the presence of appreciable amount of Cl^- and SH^-.

MeHgOH is a concerning species as it is well known to be ingested by various species of fish and will accumulate within their tissues.[12,13] The reason behind this trend is the complex formed from MeHgOH and cystine, a thiol based amino acid, which will retain MeHgOH in the tissues. This high bioaccumulation effect has led to WHO setting guidelines one the amount of mercury contaminated fish consumed, as over a lifetime too much consumed can lead to mercury poisoning.[14] Many major effects come from mercury poisoning, such as central nervous system damage, fertility damage, and cardiovascular issues. Compared to dimethylmercury, MeHgOH is significantly more dangerous because of the amount that can be consumed from eating contaminated fish.

Determining the fate of MeHgOH in aquatic environments is important in understanding the overall global mercury contamination. Previous work has validated that dimethylmercury can readily react with hydroxy radicals to form MeHgOH.[9] The presence of hydroxyl radicals in both atmospheric and aquatic environments illustrates the need to study these interactions. The interaction between $MeHg^+$ and hydroxy radicals is not well studied to the author's knowledge. I aim to study this interaction further using *ab-initio* methods to see the possible outcomes of this reaction. Six possible reaction channels are present in this interaction:

Reaction Channel 1: $MeHgOH + \bullet OH \rightarrow CH_3OH + \bullet HgOH$

Reaction Channel 2: $MeHgOH + \bullet OH \rightarrow \bullet CH_3 + Hg(OH)_2$

Reaction Channel 3: $MeHgOH + \bullet OH \rightarrow H_2O + \bullet CH_2HgOH$

Reaction Channel 4: $MeHgOH + \bullet OH \rightarrow H_2O + MeHgO\bullet$

Reaction Channel 5: $MeHgOH + \bullet OH \rightarrow \bullet MeHg + H_2O_2$

Reaction Channel 6: $MeHgOH + \bullet OH \rightarrow MeHgOH + \bullet OH$

The final reaction channel (6) is simply the reformation of the original products, but to understand the overall reaction mechanisms, this interaction will still be studied. From previous studies, it is expected that reaction channels (1) and (5) are unlikely to be thermodynamically accessible.[15] My hope is to further the interest in the study of organic mercury with high energy species, as little information on this interaction exists.

The optimal geometries for the transition states, reactants and products will be determined using density-functional theory (DFT). The energies of each reaction channel will be studied using both DFT and coupled-cluster theory (CCSD).

Quantum Chemistry

Quantum chemistry is the study of the interactions of atoms at the quantum level. This entails using a quantum mechanical interpretation of atoms to theorize the behavior of these systems. There are three types of particles that make up atom; the positively charged protons, the neutrally charged neutrons and the negatively charged electrons. Using Coulomb's law, the electrostatic force (F) can be determined based on the distance (r) between the charged particles and the charge (q) of each particle based on Coulomb's constant.

$$|F| = k\frac{|q_1 q_2|}{r^2} \qquad \text{Eq 1.1}$$

As the distance between the particles shrink, the force between them grows. For two like charges, the force is repulsive, while two opposite charges result in the attraction of the particles. This means that nuclear-nuclear interactions are repulsive, while nuclear-electron interactions are attractive.

Bohr's original model for the atom depicts electron in orbital patterns around the nucleus. This model is a poor representation of atoms, as the electrons orbit the nucleus in a different energy levels, but not in a routine motion. A better way to describe atomic structure is an electron cloud surrounding the nucleus, with the electron having a probability of being somewhere in that cloud at any given moment. We can think of this electron cloud being a probability density, where at any point of the cloud there is a certain probability of finding the electron in that spot. This electron cloud can be described by the wave function and can be used to predict the more probable locations of the electrons. Larger atoms (those with more protons) have larger electron counts which have more electron-electron interactions. Since both electrons are negatively charged,

they repulse each other and prefer to be as far as possible from each other while being closer to the nucleus.

Using the wave function, the energy of the atom can be split into three main parts: electron-electron repulsion, nuclear-nuclear repulsion, and nuclear-electron attraction. The Schrödinger equation (Eq 1.4) uses the Hamiltonian operator (Eq 1.2 and 1.3) applied to the wave function to get both the potential (V) and kinetic (T) energy of the specific wavefunction.

$$\hat{H} = \hat{T} + \hat{V} \quad \text{Eq 1.2}$$

$$\hat{H} = -\frac{h^2}{2m}\nabla^2 + V(\boldsymbol{r}, t) \quad \text{Eq 1.3}$$

Applying the Hamiltonian to a wave function is no easy task however, as there are time dependencies that must be factored in. Currently, the only system that can be solved analytically using the Schrödinger equation is the hydrogen atom. For all systems larger than this, an approximation must be made to take time out of the equation, leading to the time-independent Schrodinger equation (Eq 1.5).

$$ih\frac{d}{dt}|\Psi(t)\rangle = \hat{H}|\Psi(t)\rangle \quad \text{Eq 1.4}$$

$$\hat{H}|\Psi\rangle = E|\Psi\rangle \quad \text{Eq 1.5}$$

This approximation assumes the wave function to be stationary standing waves, making it less resource dependent to solve. As systems get larger, more interactions must be considered making even the time-independent Schrödinger equation time consuming to solve. Consider a larger atom like carbon for example, with 6 protons, neutrons, and electrons. Every electron interacts with every electron and proton, while every proton interacts with every electron, proton, and neutron, causing the number of interactions to

grow to uncalculatable levels. This led to molecular interactions needing to be approximated into much more manageable calculations.

Of these approximations, the Born-Oppenheimer approximation (Eq 1.6) is one of the most important for computing energies, as it assumes that the energy of a molecular system can be split into its electronic, vibrational, rotational, and nuclear spin energies. The approximation relies on the fact that the speed of the electron is orders of magnitude faster than the nucleus, allowing them to be separated. This allows for the energy of each interaction to be calculated independently of each other then later summed to give the total energy of the system. This approximation applied to the Schrödinger equation is the basis of modern computational and theoretical chemistry.

$$\Psi_{total} = \psi_{electronic}\,\psi_{nuclear} \qquad \text{Eq 1.6}$$

Molecular Vibrations

Covalent bonds occur when two atoms "share" electrons between themselves to create an optimal lower energy state such as a stable molecule. While these bonds have an optimal distance between them, sufficient energy can induce these bonds to extend or shrink which is known as vibrations. These vibrations are akin to a spring that is governed by Hooke's law. For a simple molecule, such as H_2, both atoms will have a vibrational mode associated which has the bond stretching and shrinking. To have this vibration occur, there must be sufficient energy input to allow the bond to extend or contract from its equilibrium position. When no energy is input to the molecule, the bond will not vibrate. Plank's equation, $\Delta E = h\nu$, correlates the energy to the vibrational frequency, determining the amount of energy required to induce the vibration. For example, H_2 has a vibrational mode for the stretching of the H-H bond of around 4000 cm^{-1}. Using the speed of light 2.98×10^{10} cm s^{-1}, this value can be converted to a frequency of 1.2×10^{14} s^{-1}. Using Plank's equation, $\Delta E = (6.626 \times 10^{-34}\ Js)(1.2 \times 10^{14}\ s^{-1})$ we

get the total joules of energy required for this vibrational mode to occur to be $7.9x10^{-20}$ J. Since most ultraviolet and visible light is well above this energy, the light from the sun is enough to induce this vibration. If enough energy is input into the system, the bonds can be induced to break, as the vibrational energy will overcome the force that keeps the atoms attracted to each other. For H_2, the bond dissociation energy is 436 kJ mol^{-1} which means for every mole of H_2 present, it takes 436000 J to break all the H_2 bonds. The energy required to break one of these bonds is $7.2x10^{-19}$ J and using Plank's equation, the vibrational frequency associated with this energy is $1.1x10^{15}$ s^{-1}. Since most visible light is within the 10^{14} s^{-1}, visible light is unable to ionize H_2, while ultraviolet light will be able to ionize hydrogen gas. While certain light can be used to break many bonds, energy can come from different sources such as heat or molecular collisions.

Collision Theory

When two atoms or molecules collide with each other, energy from this collision can be imparted to the bonds causing them to vibrate depending on how much energy was caused by the collision. If sufficient energy is imparted, atomic bonds can be induced to break which is the basis of how many reactions work. This requires the molecules to collide with each other, otherwise no energy can be imparted. For instance, if two molecules are by themselves in a large vessel, the probability of these molecules colliding is incredibly low, meaning a reaction is unlikely to occur. If there is a high density of molecules, more collisions are likely to happen leading to a higher probability of reactions occurring. This is the basis of collision theory. The rate of collision is proportional to the density of each molecule in a space, such that if more molecules are present more collisions will occur. For a bimolecular reaction, the rate of collisions is [$r = n_A n_B$] where n is the density of each reactant. Not all these collisions will have enough energy to induce a reaction to happen, and this energy is known as the activation energy

of the reaction. Thus, a probability of having the correct amount of energy must be added to the equation to determine both the number of collisions that occur and how many of these collisions lead to a reaction. The number of interactions that have sufficient energy to overcome the barrier is given by $e^{-E/RT}$ where E is the activation energy, R is the gas constant and T is the temperature in Kelvin. Combining both ideas gives us the final number of interactions that can yield a reaction given by the bimolecular rate equation (equation 1.7).

$$r(T) = k[A]^x[B]^y = \frac{k_B T}{h} e^{-\Delta G/RT}[A]^x[B]^y \qquad \text{Eq 1.7}$$

This equation is important in understanding the speed at which most reactions occur and can help determine the most probable reaction channel based on the activation energy. If the activation energy of the reaction can be determined, then the expected rate constant can be determined without using any experimental data. The rate constant of a bimolecular reaction can be determined using only theoretical data with the bimolecular rate constant equation (equation 1.8).

$$k(TST) = \kappa(T)\frac{k_B T}{h} e^{-\Delta G/RT} \qquad \text{Eq 1.8}$$

Applying this equation to equation 1.7, it is easy to see that an increase in the rate constant leads to the reaction occurring faster. This also means that if reaction channel A has a faster rate constant than reaction channel B, then A will occur faster than B. According to equation 1.8, it can also be inferred that a smaller activation energy increases the rate of the reaction exponentially. This will be the basis I use to determine which of the reaction channels studied will be most likely to occur.

Potential Energy Curves

As noted earlier, the distance between nuclei and electrons is important in determining the energy of a system. Most molecular systems have optimal configurations based on the amount of interaction of electrons and nuclei, where energy is the lowest. This spot is known as a local minimum and is where the repulsiveness of the nuclear-nuclear interaction is balanced with the attractiveness of the electron-nuclear interaction. If the internuclear distance increases the energy of the system increases due to the attraction of the nuclear-electron interaction, and if the internuclear distance decreases the energy of the system increases due to the repulsion of the nuclear-nuclear interaction. This point denotes the optimal distance between two nuclei and typically corresponds to atomic bonding. This point can be computationally found by plotting a first-derivative calculation of the energy along the potential energy surface, where if the internuclear distance changes in either direction the first derivative of the change will be positive meaning an increase in energy. At the same time, a point along the reaction coordinate in which the energy is the highest is known as a saddle point, where the first derivative of the energy on both sides is negative. The use of molecular calculations that consider the first derivative changes made geometry optimization possible. Geometry optimizations allow for finding optimal bond lengths for a saddle point or local minimum.

These stationary points can be confirmed by using analytical second derivative calculations to measure vibrations for each bond. These vibrations are important in the energy calculations and determining the type of stationary point that has been found. If all vibrations are real or positive, then a local minimum has been found. At saddle points, there will typically be one negative or imaginary frequency denoting a transition state. If a true transition state has been determined the imaginary frequency will be the bond breaking or forming route and visualization of this vibration will typically describe the

motion seen in the reaction coordinate. This imaginary frequency means the energy of the vibration is enough to overcome the bonding energy and move to a new structure.

Using the energies for each point as the internuclear distance changes, a potential energy surface can be created. This potential energy surface can be used to show the optimal path between the local minimum that pass through a saddle point if one exists. While potential energy surfaces are 3-dimensional plots with the lowest sections being the optimal paths, most times they are 2-dimensional representation. When the reaction coordinate is plotted against the energy of the system, and intrinsic reaction coordinate is formed. There will be points that are local maximum, being the transition states and local minimum being the products, reactants, or reaction intermediates. Intrinsic reactions coordinates (IRC) can be helpful to determine the reaction channel that a given transition state corresponds to. Intrinsic reaction coordinate calculations will be used to verify the correct transition state determined by Gaussian.

Computational Chemistry

With the emergence of faster and more powerful computers, computational methods for modeling chemical interactions have become a more viable option. Better algorithms for modeling the internuclear and nuclear-electron interactions have been introduced allowing for more accurate models to decrease the discrepancy between the real-world experimental values and computed values. Due to the complexity of the Schrodinger equation, all but the simplest models require approximations so they can be solved.

Two main types of computational quantum chemistry exist: *ab-initio* and semi-empirical methods. As the name suggest, semi-empirical methods include experimental data to help increase the calculations efficiency. This method saw broad use in quantum chemistry's infancy, as it could be computationally less demanding to approximate

quantum interactions. This is in stark contrast to *ab-initio* methods that rely on only theoretical approximations. *Ab-initio* methods can be more accurate than semi-empirical methods and have seen a rise in use as the computational power has increased.

A notable early *ab-initio* approximation is the Hartree-Fock (HF) method. This method uses a self-consistent field assumption which require the final charge distribution to be self-consistent with the initial charge distribution. This led to inaccuracies in computation of more complex systems. This method also neglects all relativistic effects compounding the inaccuracy applied to more complex systems. The main draw to this method is the speed of computation that can be run, requiring minimal computational power. With the increase in computational power available, stronger approximations were incorporated into the HF method to include the relativistic effects.

One of the most used methods for quantitative results is coupled cluster theory. This method integrates many-electron theory to create wavefunctions to better approximate inter-atomic interactions. This wavefunction method leads to better approximation of electron interactions and more accurate energies. Due to the complexity of creating wavefunctions computationally, the time to compute rises, increasing the cost. Though the cost is higher, it is currently regarded as one of the best methods for accurate energy approximation and is the current standard method used for energy approximations. Couple cluster theory (CCSD) includes different levels based on the inclusion of more excitations (clusters). As the number of excitations increase, the approximation becomes more exact, while requiring more electrons to be correlated at the same time. This drives up computational time but leads to more exact approximations. While times to compute single energies a decade ago could be days long, the current supercomputing clusters can give results in less than an hour for small systems.

To try and quell the high computational cost found using CCSD, Density Functional Theory has seen a rise in popularity for its low cost and highly accurate approximations. Walter Khon, Pierre Hohenberg and Lu Jeu Sham developed an approximation using the external potential created by electron densities, rather than computing the full wave-functions. This allowed them to take the most time-consuming part of the calculation, the wavefunction, and approximate it as one-electron correlations rather than the full wave-function using a local-density approximation (LDA). LDA is an approximation method that calculates the energy at each specific point in space based on the electron density at that location. The more electron density the higher the energy of that location and vice versa. Integrating the energy of all these locations can give the approximated total energy of the system. This allows for faster calculations with minimal loss in accuracy. DFT has many different levels of theory based on the amount of Hartree-Fock exchange and the DFT exchange correlation is used. Is this study, the Minnesota functional M06-2X is used. M06-2X uses a 54% Hartree-Fock exchange with the rest being the DFT correlation. This higher amount of HF exchange gives a better result when compared to those with less HF exchange (M06). This functional was chosen for being the most accurate in the M06 family while also not being too computationally demanding. While slightly less accurate than methods such as CCSD, the computational cost is magnitudes lower making DFT a strong contender for use in *ab-initio* calculations.

I used DFT methods to optimize geometries as these calculations can be completed within a few hours, and I used CCSD to calculate the energies of each point to get the most accurate approximation of the energy. Even though single point energy calculations are of the lowest computationally demanding, time to calculate with CCSD is still upwards of days to calculate each stationary point.

CHAPTER II:

LITERATURE REVIEW

Purpose

Mercury is a toxic material that is present in different ecosystems, thus it is important to investigate the speciation and fate of mercury. The amount of mercury present is well known; however, the fate of certain mercury species is not well understood and is currently being studied. Organic mercury is one of the most toxic and dangerous forms of mercury and needs more studies to investigate its production, degradation, transportation, fate, and environmental impact. While other forms of mercury have been studied experimentally and computationally, organic mercury has seen few studies with highly reactive species. Three main topics will be covered in this literature review: organic mercury in the environment, theoretical studies of mercury and methylmercury hydroxide interactions.

Mercury as an Environmental Contaminant

Mercury is a highly toxic heavy metal that has found its way into the environment through various sources and pathways. It is well known that most mercury found in the ocean is typically deposited from airborne sources such a volcanos or coal burning.[16] It is assumed that Hg(0) is converted to Hg(II) in the atmosphere leading to it falling out of the air and depositing in the soil or in water.[17]

Typically, inorganic Hg(II) is found as $HgCl_2$, which gets readily deposited into the ocean, which can further be transformed into the more dangerous form of mercury, organic mercury.[18] One possible pathway of conversion is through acidic interaction of organic materials with $HgCl_2$. This was noted in the difference between two river systems with different sediment make up.[19] The more acidic and organic containing sediment of the Wisconsin river showed more prevalence of methylmercury over the Fox river which

has a more basic composition. This study was preliminary and compared only two different river systems, but it does give good insight into possible conditions needed to convert mercuric chloride to methylmercury. Analysis of Sweden freshwater ecosystems helped to further explain the possibility that both sediment and organisms can convert inorganic mercury to methylmercury.[20] These studies started a large search for pathways that lead to organic mercury formation via biotic and abiotic pathways in aquatic environments. One major biotic pathway was found to include a specific bacterium *Desulfovibrio desulfuricans.* It was noted that in the presence of this bacterium with mercury, two main products were formed; dimethylmercury and bismethylmercury sulfide.[21] The bismethylmercury sulfide can then degrade further into dimethylmercury.[22]

These two interactions led Jonsson et al. to study further the mechanism of this interaction. This group studied the absorption of methylmercury along with the presence of FeS and found significant conversion into dimethylmercury after only 1 hour.[6] After analyzing the effect other metals bound to the sulfur, it was concluded that the makeup of these sulfur compounds made little effect on the amount of conversion. A proposed method for this interaction has two methylmercury molecules interacting to form HgS_2 and dimethylmercury. This theory is heavily supported as a mechanism for formation of dimethylmercury in the aqueous medium, as the presence of Fe^{2+} and S^{2-} in sedimentary layers forms FeS. This compound can also be found in bacterium such as *Desulfovibrio desulfuricans* further supporting their method. These pathways help to further explain the bioaccumulation effect mercury has, as most mercury consumed by humans is organic mercury[23].

Approximately 80% of the methylmercury consumed by humans comes from fish that have absorbed various forms of methylmercury.[13] Methylmercury has a strong affinity for sulfur making the more likely absorption mechanism is binding with cystine,

a sulfur-based protein in the fish muscles. Most methylmercury is found in the form Me-Hg-X (X = Cl, Br, OH) which is most readily absorbed into fish.[13] The methylmercury then binds to cysteine, forming MeHg-Cysteine. Fish native to Iran had average concentrations of methylmercury at 10 ug/kg with nearly complete absorption of this methylmercury after consumption by humans.[24] Upon consumption of methylmercury, it is absorbed into the blood via hemoglobin and is transported to the central nervous system.[26] It can pass through the blood brain barrier and cause neurological damage.[26] Methylmercury can lead to many other health effects ranging from cardiovascular effects, immune system effects, reproductive issues and even cancer.[25]

Methylmercury has been shown to be dangerous to humans when consumed and has high bioaccumulation effect in aqueous ecosystems. Studying the formation and degradation of methylmercury is extremely important as it will help understand the fate and degradation pathways of organic mercury.

Computational Studies of Mercury Compounds

Mercury compounds are of interest to study computationally as mercury's electronic configuration causes many anomalies to occur. Many computational studies of mercury try to determine the fate of mercury in the environment using predictive models. Progress has been made in the atmospheric chemistry of mercury, determining how mercury transforms in the air.

One pioneer in this field is Theodore Dibble who studied various halogenated mercury species. In 2012, Dibble et al. studied the interactions of both ClHg and BrHg radicals with free radical species in the atmosphere.[27] The goal of this work was to determine the most likely path of formation of Hg(II) compounds, as Hg(II) is the most often deposited forms of mercury.[29] A major implication of this study was the formation of XHgY compounds (X = Cl, Br ; Y = NO, NO_2, HO_2, ClO, BrO) and which one of

these has stronger bonding. This study found that the identity of X was of little importance to the strength of the Hg-Y bond. Stable compounds were formed with NO_2, ClO, BrO, and HO_2 while NO does not form a stable bond. This helps to further predict that these reaction pathways can lead to the formation of Hg(II) compounds being a possible pathway for deposition of mercury.

To further expand on the 2012 study, Lam et al. studied the kinetics of the reactions of the Br-Hg radical with both NO_2 and HOO.[29] All three reactants are easily found in atmospheric conditions and thus the interaction between them can lead to possible outcomes for mercury. Using density functional theory and coupled cluster theory, they were able to predict the rate of the reaction for each channel. The expected reaction channel was for NO_2 to add the Hg(I) and create the final product BrHgONO. A competing channel was discovered that lead to Hg(0) and $BrNO_2$ which leads to better atmospheric mercury retention. The reaction channel for BrHg and HOO leads almost exclusively to BrHgOOH as the energy of formation is nearly -40 kcal mol^{-1}. These two reaction mechanisms give a good insight to possible outcomes of atmospheric mercury.

Further study into the fate of the previously determined BrHgONO was carried out by Lam et al. in 2019.[28] Following the formation of BrHgONO the authors suspect that this molecule can undergo photolysis to form BrHgO radicals. This process starts with the excitation of BrHgONO and the excited state of BrHgONO can dissociate into BrHgO radicals and NO. The dissociation energy barrier was extremely small at 1.2 kcal mol^{-1} and the authors noted that it was nearly barrier-less based on the comparison to the dissociation of HONO (3.7 kcal mol^{-1}). After formation of the radical species, three main routes were determined to follow. The reaction with NO reforms the initial reactants which can then undergo the same reaction again via excitation with light. In the presence of hydrocarbons, BrHgO radicals will abstract a hydrogen to form a thermally stable

BrHgOH. Both CH_4 and C_2H_6 were studied using CCSD(T) with BrHgO + CH_4 having a barrier less reaction (-0.7 kcal mol^{-1}) and BrHgO + C_2H_6 having a small energy barrier (2.6 kcal mol^{-1}). BrHgO + NO_2 has a barrier-less reaction with a total loss in energy of 58 kcal mol^{-1}. Due to the overall abundance of methane in the atmosphere compared to both NO and NO_2, the authors expect BrHgOH to dominate over the other two possibilities. These studies help understand the flow of mercury from the source to atmospheric deposition of mercury into different ecosystems.

While there are many theoretical studies on atmospheric formation of Hg(II) species, studies into the interaction and formation of methylmercury are limited. The methylation of mercury was studied using halogenated methane and light to for MeHgX (X=halogen).[30] Using Density Functional Theory, the formation of methylmercury without the presence of biotic systems requires a large amount of energy into the system (+39 kcal mol^{-1}) making it thermodynamically improbably to occur. It was noted that the introduction of light could speed the reaction up, but not to the point to make this reaction a viable source of MeHgX. A possible pathway for the formation of Me_2Hg was found using $[CH_3ClCH_3]^+$ which was more thermodynamically accessible (7.9 kcal mol^{-1}) due to the reactive nature of dimethylchlorinium. The reaction is slightly endothermic with the products being 4.7 kcal mol^{-1} higher than the reactants. While the possible ecological impact of this reaction is minimal, it further supports the need for biotic or abiotic methylation using sulfur containing reactants.

Most current theoretical work on organic mercury study the stability of methyl or dimethylmercury in various situations. Shagun et al.[31] studied the complexation of methylmercury cations with different ligands. Upon analysis, the strongest bonding ligands were selenium, sulfur, and chlorine ligands. Bonding to OH ligands showed the weakest bonding. This has deep applications to mercury based medical solutions, not

necessarily the fate of mercury in the environment. This does have implications environmentally noting that when mercury bonds to sulfur-based groups, mercury is less likely to dissociate compared to OH ligands.

Lee et al.[32] studied the thermochemistry of methylmercury and the bond dissociation energies using DFT and CCSD(T). Using the Becke-3 Parameter Lee-Yang-Parr correlation (BLY3P), the optimized bond length for MeHg was around 2.4 angstroms with the CCSD(T) bond lengths being extended to over 3.0 angstroms. For all levels of theory, the C-H bong lengths were similar at 1.08 angstroms. The dissociation energy for HgMe to Hg + CH_3 found using CCSD(T) is 5.7 kcal mol^{-1}. $MeHg^+$ was found to have a bond length of 2.1 angstroms at all levels of theory with the same C-H bond length of 1.1 angstroms. The dissociation energy for $MeHg^+$ is around 60 kcal mol^{-1}.

The stability of dimethylmercury in environmental conditions is important to understand the global mercury cycle. Dimethylmercury's stability with aqueous species was studied by Bytautas[8] to give a better understand of its reactivity. Dimethylmercury showed small amounts of complexation with H_2O with higher complexation to NH_3 which the author noted could be due to NH_3's more alkaline nature. This result is confirmed by testing the same complexation with Cl-Hg-Cl as both H_2O and NH_3 showed higher levels of complexation to the partial charges formed in Cl-Hg-Cl. Complexation of MeHgMe with ^-OH resulted in much lower energies in high pH situations as ^-OH helped stabilize dimethylmercury. In low pH situations, H_3O^+ readily reacted with dimethylmercury creating $MeHgOH_2^+$ meaning low pH situations helped degrade dimethylmercury. Other ionic ligands such as Cl^- and NH_4^+ helped to further stabilize dimethylmercury.

Theoretical studies of mercury primarily focus on the atmospheric reactions with highly reactive gaseous species. Many possible sources of Hg(II) from different inorganic

mercury compounds have been discovered, helping determine the route mercury takes from expulsion into atmosphere to deposition into aquatic environments. Studies have also been covered that show the process of methylation of mercury once in these aquatic environments, but the fate of dimethylmercury has not been studied intensively. Few theoretical studies for dimethylmercury's interaction with high energy species exist. With my research, I hope to spark interest in these interactions as possible pathways for dimethylmercury.

Methylmercury Hydroxide's Environmental Impact

Methylmercury, which is often used and a generic name for mono-methylmercury compounds with $MeHg^+$, is of the greatest concern because it is high toxicity, mobility and its ability for bioaccumulation and magnification in the food web. Human exposure today occurs almost exclusively from consumption of fish and marine mammals.

Methylmercury hydroxide is an important species in aquatic bioaccumulation of methylmercury. With the dangers that come from methylmercury, knowing pathways in which methylmercury changes in the environment is important. There are studies into both the stability and the possible degradation pathways of methylmercury. Very few reports could be found on the interactions of methylmercury and high energy species such as the hydroxyl radical.

Shagun et al.[31] investigated the complexation of $HgMe^+$ with various ligands in aqueous solutions. It was determined that the strength of the Hg-C bond decreased as the size of the ligand increased. This means the Hg-C bond is weaker in MeHgCl than in MeHgOH, and thus can dissociate faster. It was concluded that the Hg-C bond could be weakened by the presence of an organic RS or RSe ligand.

Mono-methylmercury has been reported in artic seawaters, and the source of this contamination is unknown. Kirk[33] took samples from various regions of the ocean and

found high levels of dimethylmercury at lower depths of the ocean while surface amounts of dimethylmercury were low. This coincides with other literature that the conversion of mercury to dimethylmercury occurs at the sedimentary level rather than at the oceanic surface. It is predicted that dimethylmercury should photo-dissociate into methylmercury as it approaches the surface, leading to less concentrations of dimethylmercury near the surface. Methylmercury levels are expected to be higher near the surface, where most fish are contaminated.

This analysis is supported by the breadth of literature showing the photodegrading potential of the Hg-C bond. In 1998, Tossell[11] utilized Hartree-Fock and Moller-Plessett second order perturbation (MP2) theories to study the degradation of mono-methylmercury complexes to find the required input energy to dissociate. It was found that the transition of the singlet to triplet excited state for both $MeHgOH_2^+$ and MeHgSH required energies that could be possible with solar radiation (~4 eV). The triplet state of $MeHgOH_2^+$ were shown to dissociate into CH_3 and $HgOH_2^+$ radicals and the triplet state of MeHgCl dissociated into CH_3 and HgCl radicals. This is due to the excited state causing the Hg-C bond to elongate making it more likely to break. The reaction between MeHgCl and ^-OH has a reaction energy of -20 kcal mol^{-1}, making MeHgOH far more stable than MeHgCl. The reaction between MeHgOH and SH^- has a reaction energy of +126 kcal mol^{-1} making MeHgSH far less stable than MeHgOH. Through the reactions studied it was determined that both MeHgOH and $MeHgOH_2^+$ are the main species present in aqueous medium as they are the most stable compounds out of the studied complexes. This research illuminated the theoretical background for the photodissociation of methylmercury compounds.

Photo-degradation of MeHg species is also supported by Pan et al.[34] and their study on the presence of MeHg on the Wen-Rui-Tang River. Samples were collected

from various sites upon the river system including locations with higher industrial presence and at different times of the year. High-performance liquid chromatography was used to determine the amount of MeHg species present in each sample. The highest concentrations were found in the industrial areas near wastewater dumps in the wintertime. This helps to determine that most mercury contamination present in the rivers are from industrial dumping. The interesting result comes from the amount present in each season. The highest presence of MeHg in most cases comes in the winter and spring time, with the summer being the lowest concentration of the seasons. Several factors could play a role in this result, but the most interesting factor is the amount of sunlight in each season. In the summertime, more sunlight is present due to longer days and the sun being closer to the earth. With the general acceptance of photodissociation of MeHg being possible, this lends to the summer having more sun causing more MeHg to be dissociated while other seasons see less sun and thus less dissociation. While this study has flaws such as little control for more dumping occurring, it does help to support photodissociation of MeHg being a significant pathway.

The reaction between MeHgCl and OH radicals has been studied experimentally to determine the importance of this pathway. Chen et al.[35] utilized a Xenon lamp to create hydroxyl radicals to react with MeHgCl at a pH of 5. Dithizone was used as the detection method, as in the presence of mercury a complex is formed that absorbs at 496 nm. Using Beer's Law, the amount of Hg could be determined by the absorbance at 496 nm against the reference beam. Absorbance over set time intervals was studied to determine the rate constant of the reaction. The second order rate constant of 9.83×10^{9} M^{-1} s^{-1} (1.63×10^{-11} cm^{3} $molecules^{-1}$ s^{-1}) was found for the overall reaction. With this high-rate constant, this interaction is thermodynamically accessible and warrants further study of MeHg compounds with hydroxyl radicals.

CHAPTER III:

METHODOLOGY

Using Gaussian

All *ab-initio* and density function theory calculations in this study were carried out using Gaussian 09 and Gaussian 16.[36-38] Gaussian 09 was used on local computer systems at UHCL, and Gaussian 16 was used on the Bridges2 supercomputer courtesy of XSEDE. Gaussview5 was used to create input files for operation with the Gaussian systems. Input files include the cartesian coordinates of all atoms in the system so that the Hamiltonian matrix can be created based on these positions. Input files also contain the information on the type of test being conducted. Certain keywords must be included to ensure proper results are obtained based on the type of calculation. To calculate single point energies, no keyword needs to be used as single point energies are the default method. To run a second derivative frequency analysis, the keyword "freq" is used. Modifiers to this keyword can be added, such as "noraman" to have Gaussian not consider the Raman frequencies. Typically, no modifiers are added to the frequency analysis as none are needed. To calculate the optimized geometries, the keyword "opt" is used and modifiers are added based on the type of optimization to be determined. A modifier that must always be added is the type of force constant calculations to be used. "calcfc" signifies that Gaussian should calculate the initial force constants at the beginning and use the same force constants through the whole optimization. This specification can be used to shorten calculation times while slightly decreasing accuracy. For all geometry optimizations, the keyword "calcall" were used to signify that Gaussian should recalculate force constants after every optimization. Setting "opt=ts" instructs Gaussian to use the Berny optimization method to find a saddle point or a transition state. To run an intrinsic reaction coordinate, the keyword "irc" must be used along with the

force constant keyword. Keywords must also be added for the different basis sets and theory levels. To specify the DFT method I used, the keyword “m062x” was used along with the basis set “def2tzvp”. For single energy calculations with CCSD(T), the keywords “ccsd(t)” and “genECP” were used. genECP signifies to Gaussian that the basis set information is stored at the end of the input file. This keyword is need so that the basis sets can be split for each atom. At the end of input file, each atom must have a specified basis set applied to it, and for use with CCSD(T) carbon, hydrogen and oxygen will use the same basis set. Mercury will have an effective core potential applied that allows relativistic effects to be considered without using the full basis set. All keywords are used on the same line of the input file that starts with a “#”. Other additions to the input file can be used to specify the amount of computer cores and memory for Gaussian to take control of. These keywords are entered as “%CPU=” and “%MEM=” respectively. These have no bearing on the output file itself, rather on the amount of time required to finish the calculation. Below are two sample input files created using Gaussview5 for M06-2X calculations and CCSD(T) calculations.

Optimization Example

%mem=4GB

%cpu=0-15

opt=(calcall,noeigen,ts) geom=connectivity def2tzvp m062x

MeHgMe + OH -> MeOH + HgMe

0 2

Hg	0.30330064	0.00396225	0.00005988
C	-2.03120936	-0.01401875	-0.00004512
H	-2.10198536	0.51753025	0.93634688
H	-2.10181936	0.51808925	-0.93613412
H	-2.10880336	-1.08896175	-0.00037412
C	2.44712664	0.00546625	-0.00042112
H	2.79917064	1.02036925	-0.17173012
H	2.79987764	-0.35396575	0.96375088
H	2.79849664	-0.65015075	-0.79411612
O	-4.00854536	-0.09499175	-0.00025412
H	-4.20085936	0.85246525	-0.00015912

Single Point Energy Example

%mem=4GB

%cpu=0-15

ccsd(T,T1diag,maxcyc=100,window=(8,0)) geom=connectivity genECP

CCSD energy calculation of DMM for with AVTZ

0 2

Hg	-0.12653400	-0.07211700	0.00024700
C	-2.22104600	0.14352600	0.00002900
H	-2.70763400	-0.82291400	-0.10961000
H	-2.53985600	0.59863100	0.93589700
H	-2.51741300	0.78742500	-0.82591200
C	1.87541400	-1.02990000	-0.00188200
H	1.57615500	-2.07745700	-0.01312800
H	2.42488000	-0.76464800	-0.89888300
H	2.41760700	-0.78380900	0.90525600
O	1.40186900	1.60239100	-0.00570600
H	2.32781200	1.33125100	0.04338100

C H O

aug-cc-pVTZ

****

@/usr/local/g09/basis/AVTZ_Hg.gbs

Basis Set Information

The triple-zeta valence polarization Karlsruhe basis set, Def2-TZVP[39], was used to treat mercury, carbon, oxygen, and hydrogen for DFT. This basis set was chosen for its high accuracy and relative low cost. The Def-basis set family has support for transition metals including mercury without the need to use effective core potentials. The density function theory (DFT) method used in this study is the (Minnesota functional) M06-2X,[41] which is a global hybrid meta-generalized gradient-approximation functional with 54% Hartree−Fock (HF) exchange; it is part of the M06 family of functionals developed by the Truhlar group.

Geometry optimizations for the structures of reactants, transition states and products were optimized with M06-2X using an unpruned grid. Each structure was optimized using Gaussian's optimization sequence, being either a true local energy minimum or a Berny optimized transition state. Transition state structures were validated by the presence of one imaginary (negative) frequency, and further validated by an intrinsic reaction coordinate (IRC) calculation. The zero-point energy and Gibbs free energy corrections were determined using the harmonic oscillator approximations with an analytical frequency analysis.

Single point energy values of each species were then calculated using single, double, and triples included coupled-cluster theory (CCSD(T)).[40] The Dunning correlation basis set aug-cc-pVTZ[42,43] was used as the basis set for carbon, hydrogen, and oxygen. The small-core Stuttgart/Cologne scalar relativistic pseudopotential was used to correlate the innermost 60 electrons for mercury with an augmented triple-zeta basis set[44] to treat the outermost 20 electrons explicitly. This basis set combination will be referred to as AVTZ. The corrections found with DFT were applied to the CCSD(T) energies to get two different data sets: the electronic energy and Gibbs free energy. The activation

energies were found using the Gibbs free energy and were used to determine the rate constants.

Geometry Optimization

As noted earlier, all optimization calculations were run using the DFT method M06-2X as using CCSD(T) would be too high of a computational cost. To optimize geometries, the Gaussian keyword “opt” was used with the modifier “opt=ts” used for transition states. To optimize reactant and products, the individual structures were optimized by themselves. For optimization of the transition state, “opt=ts” was added with a relatively close approximation of the expected transition state geometry. This means placing the two molecules close to where the interactions begin to occur and using the “ts” keyword to have Gaussian search that relative area for a saddle point. If the starting geometry were not close enough to the true transition state, the run will either fail to converge, or an incorrect geometry would be found. All output geometries had to be validated using the frequency analysis to verify a single imaginary (negative) frequency. This transition state structure was then input using the “irc” keyword to have the IRC path mapped. The IRC calculation would then verify that the transition state in between the reactants and the products. If the IRC does not show the correct path, then the transition state is incorrect and the correct transition state must be found.

Rate Constant Determination

The electronic energies were calculated with CCSD(T), and a Gibbs free energy correction was applied to these values to get the Gibbs free energy. This correction considers the enthalpy and entropy of the given system, and due to the computational cost, the correction was calculated with M06-2X. The Gibbs free energy correction is calculated with the analytical frequency calculation, then added to the electronic energy.

$$\Delta G = E_{elec} + \Delta G_{corr} \quad \text{Eq 3.1}$$

The activation energy is calculated by taking the energy difference of the transition state energy and the reactant energies. Rate constants for the reaction were computed using canonical Transition State Theory (cTST)

$$k(TST) = Lk(\mathrm{t})\frac{\mathrm{k_B T}}{\mathrm{h}c_0}e^{\frac{-\Delta G}{RT}} \quad \text{Eq 3.2}$$

where L is the degeneracy of the transition state, K_b is Boltzmann's constant, h is Plank's constant, C_0 is the pressure, R is the universal gas constant, k(t) is the quantum tunneling correction, and T is the absolute temperature. The second order rate constants (in cm^3 $molecules^{-1}$ s^{-1}) were calculated assuming a standard pressure of $2.46x10^{19}$ molecules cm^{-3} at 298K. The degeneracy (L) was calculated in Gaussian based on the symmetry of the system. The Skodje tunneling approximation[45] (Eq 3.3-3.5) was used for the tunneling correction factor when appropriate [(21)].

$$k(T) = \frac{(\beta\pi/\alpha)}{\sin\left(\frac{\beta\pi}{\alpha}\right)} - \frac{\beta}{\alpha-\beta}e^{[(\beta-\alpha)(\Delta V^{\ddagger}-V)]} \quad \text{Eq 3.3}$$

$$\alpha = \frac{2\pi}{h\, Im(v^{\ddagger})} \quad \text{Eq 3.4}$$

$$\beta = (\mathrm{k_B}T)^{-1} \quad \text{Eq 3.5}$$

Where V is the potential energy for the stationary points and Im(v) is the imaginary frequency at the transition state. The Skodje tunneling approximation considers the possibility that electrons can pass through the energy barrier rather than having to overcome the activation energy typically required. These approximations will

be applied to all the of the reaction channels, even if the correction does not change the rate constants by a significant amount.

CHAPTER IV:

RESULTS AND CONCLUSIONS

Dimethylmercury Interaction with Hydroxyl Radicals

For the reaction between dimethylmercury with hydroxyl radicals, there are three thermodynamically accessible channels available. Each channel's reactant, product and transition state geometries were optimized with M06-2X with the Def2-TZVP basis set and shown below. The intrinsic reaction coordinates for each channel were also calculated using DFT and are described below. Single point energies were calculated using CCSD(T) with AVTZ and the Gibbs free energy corrections calculated using DFT were applied to these single point energies. These CCSD(T) calculated Gibbs free energies were used to create energy profiles. A Gibbs free energy (in kcal mol^{-1}) profile including all the reaction paths are shown in Figure 4.1.

Table 4.1:

Gibbs free energies and rate constants using DFT and CCSD(T) for the three possible reaction channels.

Reaction channel	M06-2X/DEF2-TVZP		CCSD(T)/AVTZ	
	ΔG[a]	k(TST)[b]	ΔG[a]	k(TST)[b]
MeHgOH[c]	7.0	2.08E-12	7.3	1.23E-12
$MeHgCH_2•$[d]	9.0	9.86E-14	8.9	1.14E-13
MeHg[e]	24.0	1.55E-24	22.8	1.05E-23

[a] Energy barriers calculated using Gibbs free energy corrections in kcal mol^{-1} *[b] k(TST) calculated using transition state theory and Skodje tunneling correction in* cm^3 $molecule^{-1}$ s^{-1}. *[c] Skodje tunneling correction=1.06 [d] Skodje tunneling correction=1.50 [e] Skodje Tunneling correction=2.31*

Comparing the rate constants for each of the reaction channels (table 4.1), there are clear differences between the three channels. The Skodje tunneling correction was applied to the rate constant for all three reaction channels. The MeHgOH formation channel saw a 6% increase due to the low imaginary frequency of 100 cm^{-1}. For the hydrogen abstraction, there is a 40% increase of the rate of reaction due to the large imaginary frequency (637 cm^{-1}) of the transition state. For the methyl abstraction reaction there is a nearly 130% increase in the reaction rate due the largest imaginary frequencies of the reaction channels at 850 cm^{-1}. This increase, however, is not significant due to the extremely high energy barrier for channel 3.

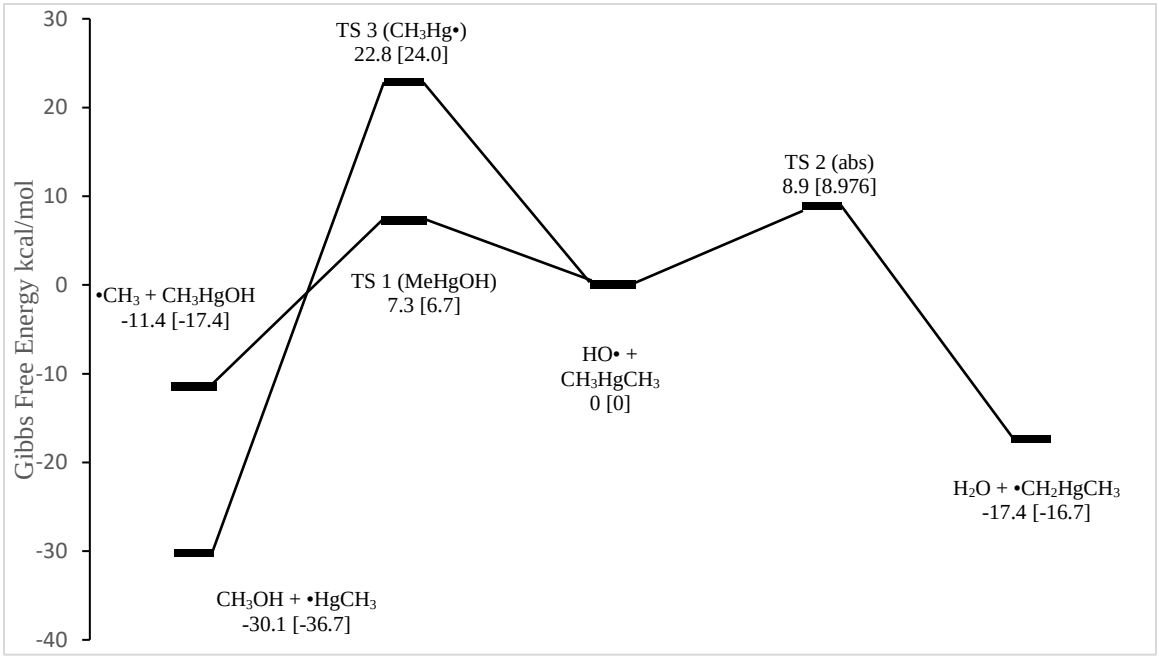

Figure 4.1:

Gibbs free-energy profile in kcal mol^{-1} for all three reaction channels of HO + CH_3-Hg-CH_3 at CCSD(T)/AVTZ (M06-2X in brackets).

Formation of MeHgOH (Channel 1)

Figures 4.2 and 4.3 show the optimized geometries for the stationary points along the reaction coordinate and the IRC determined by Gaussian, respectively. Based on the electronic energy profile, there is a pre-reactive complex that is formed between the dimethylmercury and the hydroxyl radical on the way to the transition state. At the pre-reactive complex, interactions start to occur between the oxygen and the mercury as the internuclear distance approaches 2.8 Å. This interaction also begins to push the methyl group away from the oxygen, so that the C-Hg-C angle in the complex deviates from linearity by 0.1°. The lowered electronic energy of this pre-reactive complex comes from the London dispersion forces that help to stabilize the radical. At the transition state the Hg-C bond length and angle are 2.2 Å and 160°, respectively. The Hg-O internuclear

distance is shortened to 2.3 Å, being nearly equal to the Hg-C distance. As the reaction continues, a post-reactive complex is formed in which the methyl radical coordinates nearly orthogonal to the mercury resulting in lower energy. The C-H bond extends to 3.2 Å before the methyl radical leaves. The bond length on the MeHgOH product coordinate closer to their final lengths and bond angles. The product's Hg-O bond length is 2.0 Å with an angle of 177°. Upon separation, the hydrogens on the methyl radical orient planar with a nearly 120° angle between each.

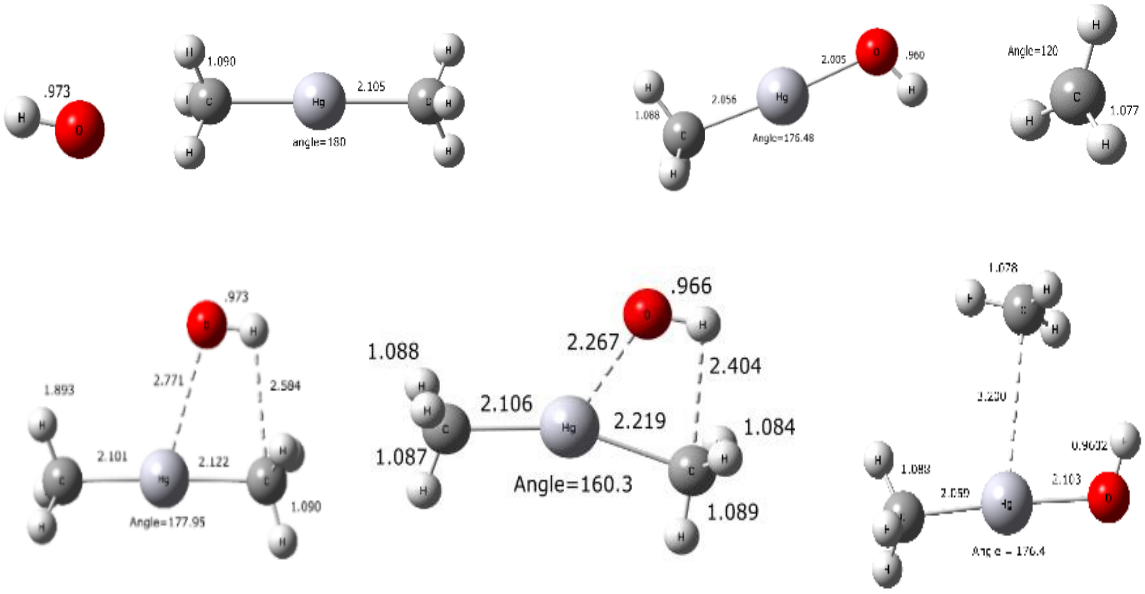

Figure 4.2:
M06-2X optimized geometries for the reactants, products, transition state and pre-reactive complex for channel 1.

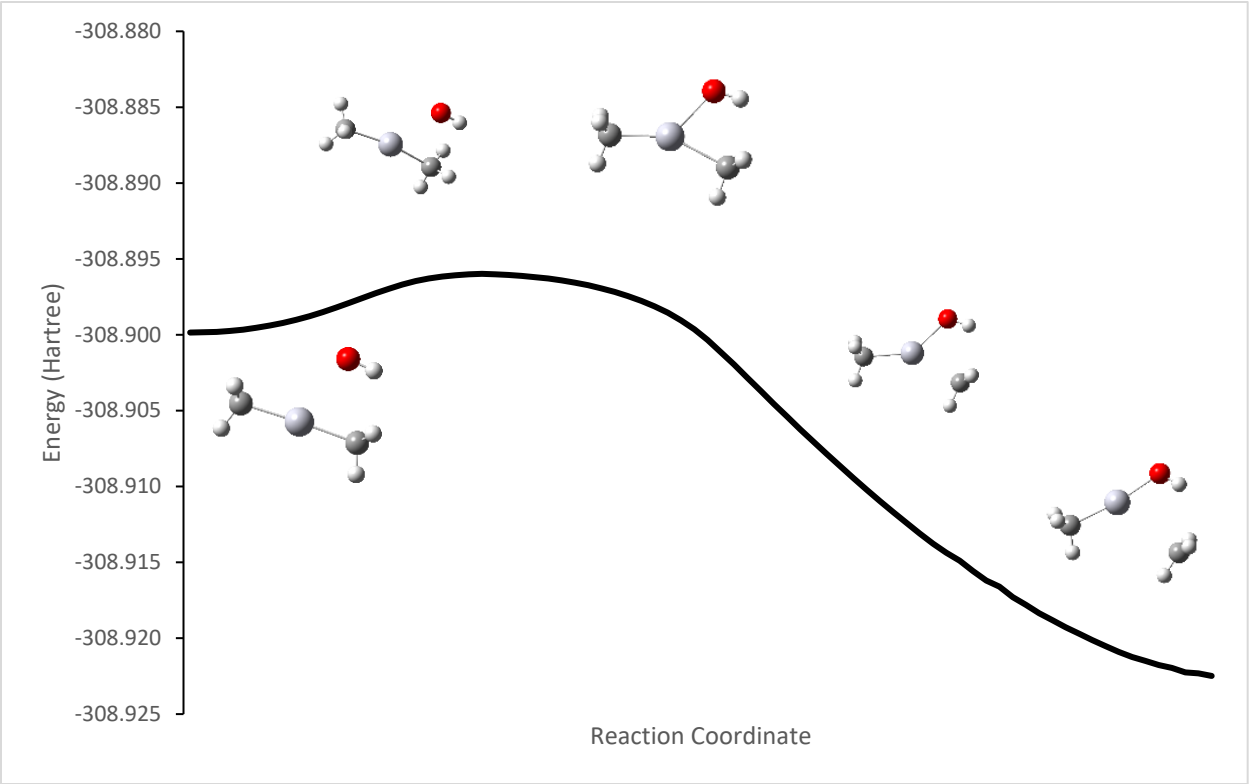

Figure 4.3:
Intrinsic reaction coordinate for channel 1 starting at the pre-reactive complex through the products.

This reaction channel is exergonic at 298 K with an overall Gibbs free energy difference of -11.4 kcal mol^{-1} for CCSD(T) and -17.4 kcal mol^{-1} for M06-2X. As shown in Figure 4, the electronic energy profile includes an energy minimum at the pre-reactive complex (PRC). However, this energy minimum is not observed in the Gibbs free energy profile. Consequently, the PRC will not be factored into the reaction rate calculation. The activation barrier for this channel is 7.3 kcal mol^{-1} (7.0 kcal mol^{-1} for DFT). This low energy barrier makes this channel kinetically accessible at 298 K and constitutes a feasible channel for this reaction.

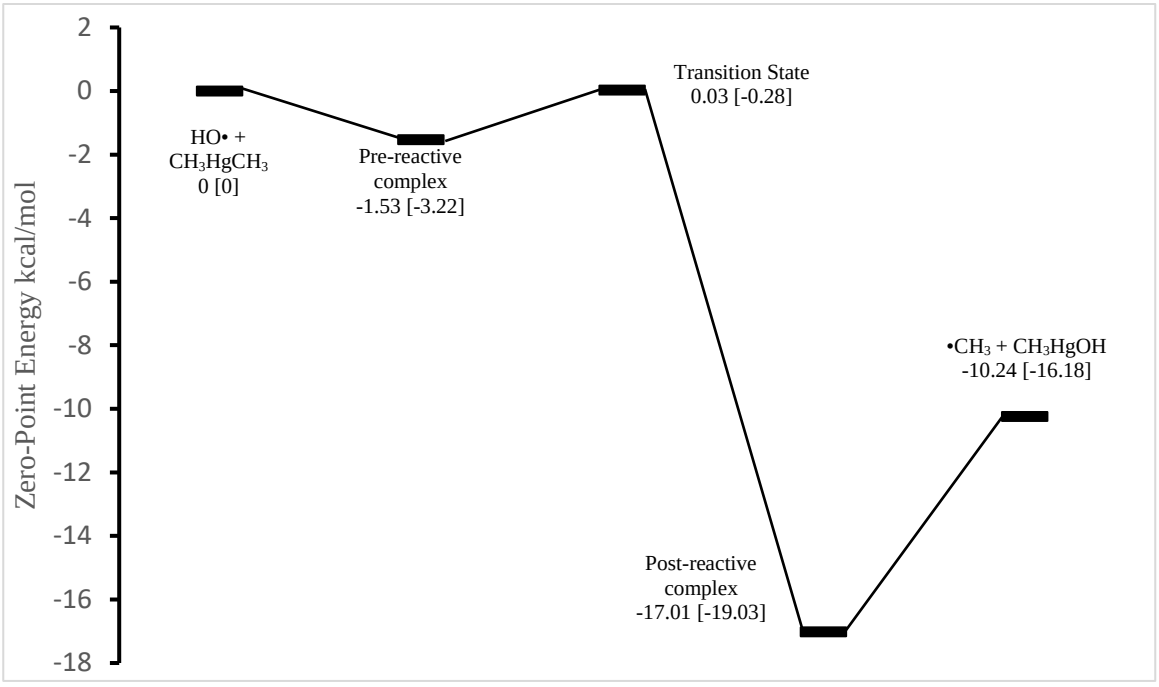

Figure 4.4:
ZPE-corrected energy profile for reaction channel 1 with energies in CCSD(T)/AVTZ and M06-2X/Def2-TZVP values in brackets.

The rate constant was determined to be 1.23 x 10^{-12} cm^3 $molecule^{-1}$ s^{-1} (2.08 x 10^{-12} cm^3 $molecule^{-1}$ s^{-1} for DFT) at 298 K. The tunneling approximation increased the rate constant for this channel by only 6% due to the low imaginary frequency for the transition state. The CCSD(T) and DFT rate constants are comparable to the experimental data collected by Niki et al.[14] as they noted the predominance of the MeHgOH formation and a rate constant of 1.97×10^{-11} cm^3 $molecule^{-1}$ s^{-1}. As the authors noted, however, MeHgOH was not able to be studied directly, thus this comparison is between the rate of formation found in this work against the rate of disappearance of dimethylmercury. Comparing the theoretical rate constant of MeHgOH formation to the experimental rate constant for disappearance of MeHgMe, the rate constant we calculated using CCSD(T) is slower by a factor of 10.

Hydrogen Abstraction (Channel 2)

Figures 5 and 6 show the optimized geometries for the stationary points along the reaction coordinate and the IRC, respectively. As the radical approaches dimethylmercury, the interaction between the oxygen and hydrogen causes the hydrogen-carbon bond to elongate. At the transition state, the C-H bond extends to 1.2 Å while the O-H bond is 1.4 Å. For the similar channel in the HO + CH_4 interaction, the bond lengths calculated were 1.2 Å and 1.3 Å for C-H and O-H respectively (using M06-2X). This corresponds well to the abstraction from dimethylmercury, with identical bond length for each. While this occurs, little change occurs to the mercury and non-interacting methyl group. The final bond length for the Hg-CH_2 is slightly shorter (-0.03 Å) than the Hg-CH_3 bond length, likely due to the charge distribution of the radical with the mercury. With the extra electron on the carbon, the bond length is shortened, allowing the radical electron to be stabilized by mercury. The C-H bond lengths vary little between the CH_2 and the CH_3.

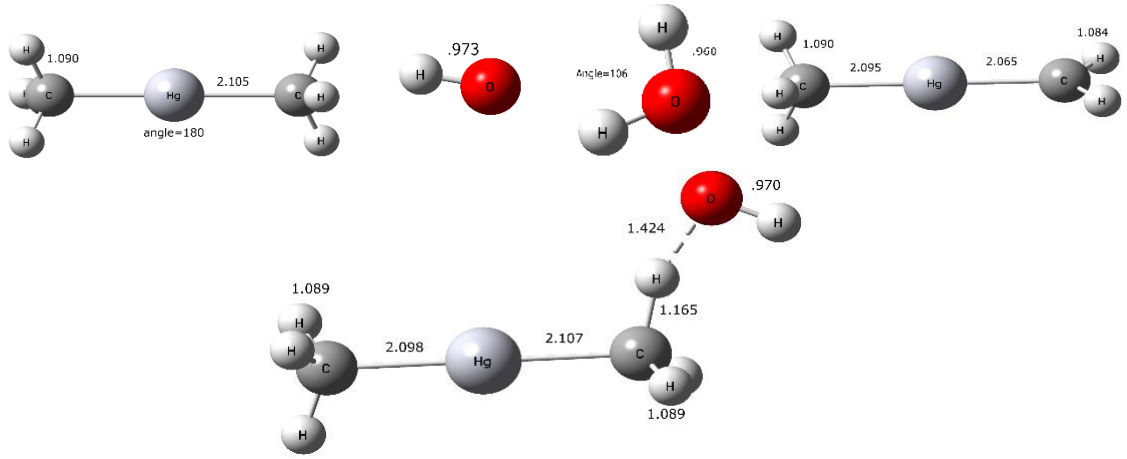

Figure 4.5:
M06-2X optimized geometries for the reactants, products, and transition state for channel 2

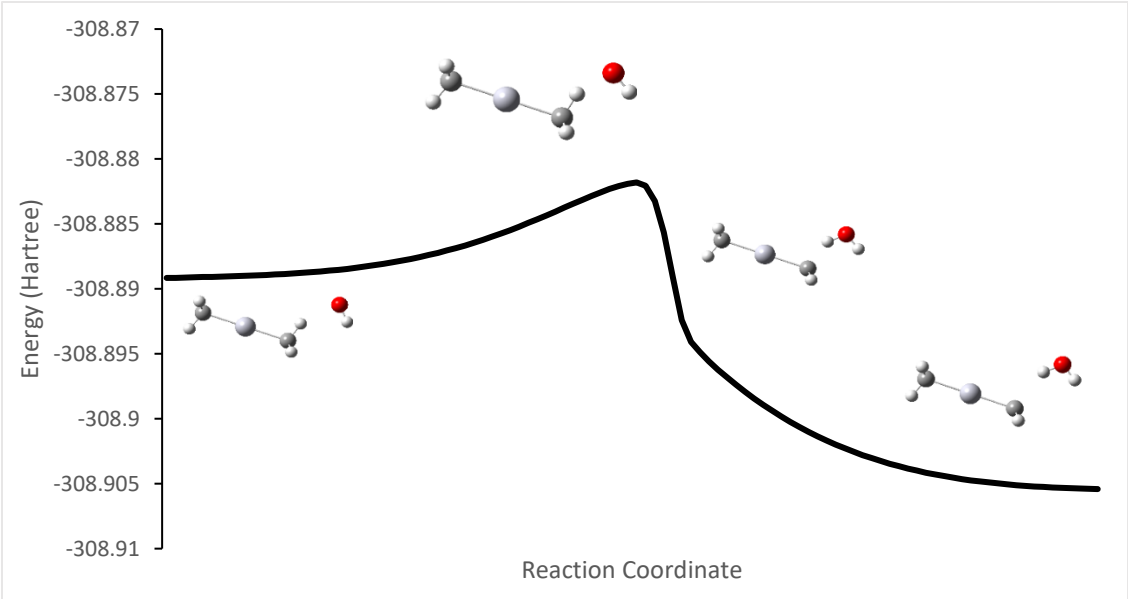

Figure 4.6:
Electronic energies along the minimum energy path for channel 2 starting at the reactants through the products calculated using M06-2X/DEF2-TZVP

The hydrogen abstraction reaction is exergonic with an overall energy change of -17.4 kcal mol^{-1} (CCSD(T) and -16.7 kcal mol^{-1} M06-2X). The two methods are in great agreement with each other, being less than a kcal mol^{-1} difference. An energy barrier of 8.9 kcal mol^{-1} was found for CCSD(t) and in good agreement with the DFT value of 9.0 kcal mol^{-1}.

As expected for a hydrogen abstraction reaction,[46,47] this channel saw a significant contribution (~40%) to the rate constant by applying the Skodje quantum tunneling approximation. This is due to the large imaginary frequency at 637 cm^{-1}. With the tunneling correction applied, the bimolecular rate constant was calculated to be 1.16×10^{-14} $molecules^{-1}$ cm^3 using CCSD(T) values (1.01×10^{-13} $molecules^{-1}$ cm^3 for DFT) at 298 K. The rate constants between CCSD(T) and DFT are in good agreement with each other and in close agreement with the literature value for the abstraction of hydrogen from methane (~1×10^{-14} cm^3).[48] While this reaction channel is not the most energetically favorable amongst the channels, it can still be expected to occur at room temperature.

MeHg Formation (Channel 3)

Figures 4.7 and 4.8 show the optimized geometries for the stationary points along the reaction coordinate and the IRC, respectively, for channel 3. The optimal path for this reaction channel is a backside attack on the methyl group by the OH radical. This can be described as an 2nd-order electrophilic substitution reaction with MeHg as the leaving group. As the radical approaches, the Hg-C bond length extends, and the hydrogens begin to orient 90° to the principal axis. At the transition state the Hg-C bond length is 2.3 Å while the opposite Hg-C bond in only 2.1 Å.

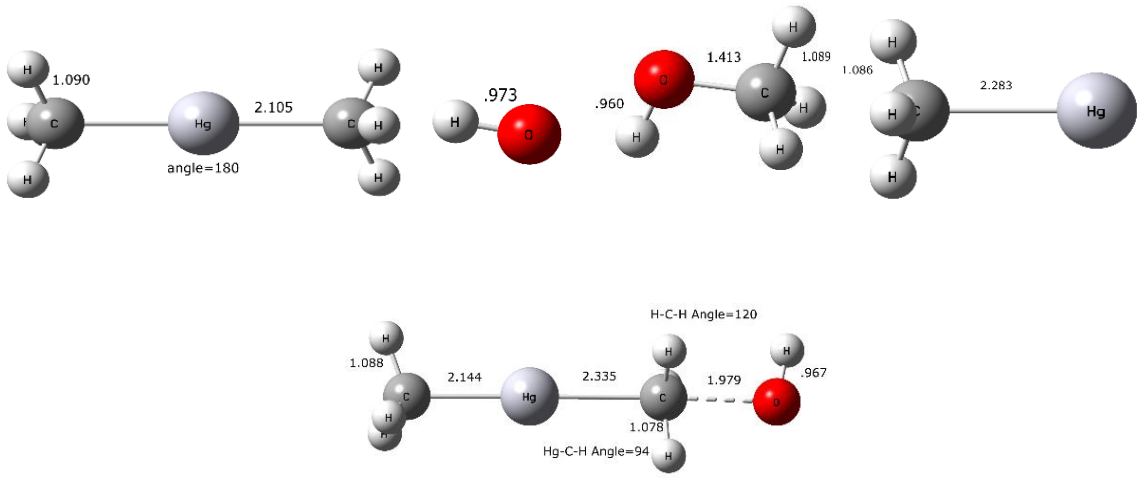

Figure 4.7:
M06-2X optimized geometries for the reactants, transition state, and products for channel 3.

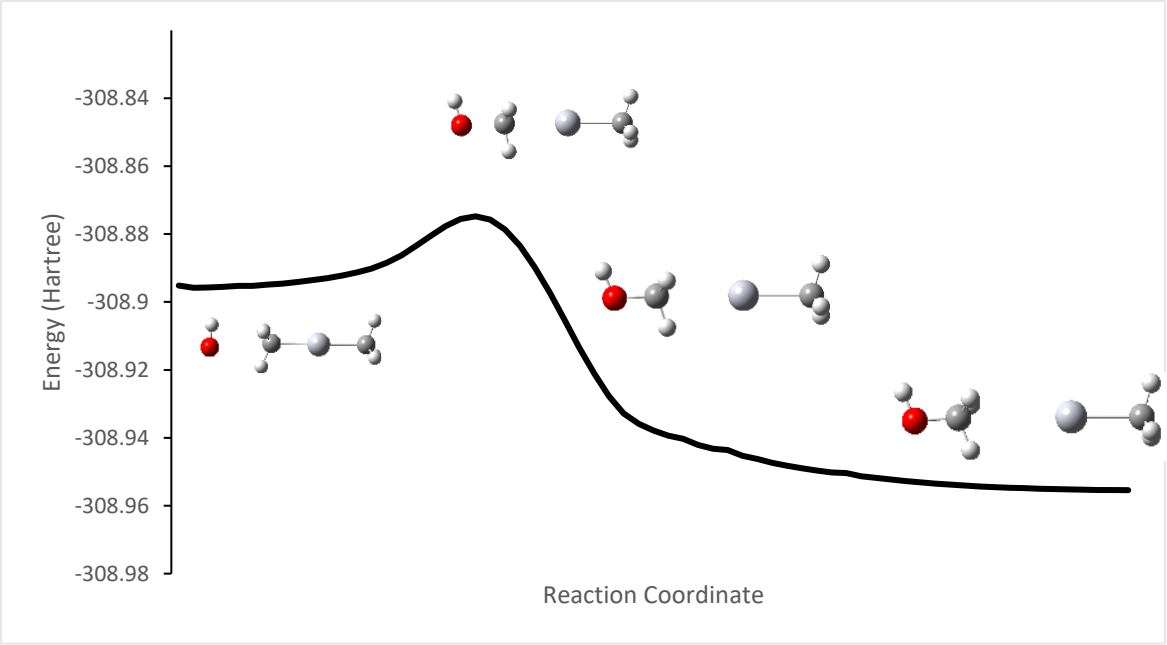

Figure 4.8:
Intrinsic reaction coordinate for channel 3 starting at the reactants through the products.

This reaction channel has a Gibbs free energy loss of -30.1 kcal mol^{-1} for CCSD(T) (-36.7 kcal mol^{-1} for M06-2X) making it the most thermodynamically favorable reaction channel for this interaction. This reaction channel is kinetically

inaccessible due to its high energy barrier of 22.8 kcal mol^{-1} CCSD(T) (24.0 kcal mol^{-1} for M06-2X). Even though the hydroxyl radical is highly reactive, this high barrier makes this reaction channel unlikely to occur and making it the least kinetically accessible at room temperature. A likely reason for this large energy barrier is due to little interaction of the OH radical with mercury at the transition state, since the attack comes from the backside.

As with the hydrogen abstraction channel, there is a large imaginary frequency ($849cm^{-1}$) leading to large tunneling effects. Even with this considered, the high energy barrier leads to a rate constant that is multiple orders of magnitude below the others. The bimolecular rate constant calculated is 1.06×10^{-23} cm^3 $molecule^{-1}$ s^{-1} (CCSD(T) and 1.55×10^{-24} cm^3 $molecule^{-1}$ s^{-1}) at 298 K. Little experimental data on this reaction channel exist, and it is likely due to low probability for this channel to occur at room temperatures. Niki et al.[14] found this reaction to not occur when done experimentally at room temperature while end products indicate the other two reaction channels occurred. From Niki's findings and our computational data, it can be inferred it is unlikely that this reaction channel has a meaningful impact on the fate of dimethylmercury in the gas phase at room temperature.

Discussion

The methyl abstraction reaction (channel 3), due to its high activation energy barrier, has the lowest rate constant with minimal chance of this reaction channel occurring under normal environmental conditions. No experimental results for this channel have been reported to the author's knowledge. The contribution of this channel to the fate of dimethylmercury should be minimum. The low energy barrier and relatively high-rate constant of the hydrogen abstraction channel (channel 2) leads to CH_3-Hg-CH_2 being a possible outcome for this reaction. Formation of CH_3-Hg-OH has the lowest

energy barrier and thus the highest rate constant, leading this channel being the largest contributor among these three channels. Our computational result is in reasonable agreement with experimental results, as Niki et al.[14] found the primary product to be CH_3-Hg-OH, the secondary product as CH_3-Hg-CH_2 and MeOH not being observed experimentally. With a rate constant 10 times faster than the hydrogen abstraction, it is expected that the formation of MeHgOH will dominate this interaction making MeHgOH the primary product which is in good agreement with the experimental outcome.

With hydroxyl radicals being a species easily created by ultraviolet light from the sun that can pass through the upper atmosphere, this leads to the possibility of hydroxyl radicals to interact with dimethylmercury and form MeHgOH. This result not only matches with Niki et al.,[14] but also with prominent studies that noted the higher levels of mono-methylmercury (MeHgX) in locations that have more UV radiation. Pan et al. and Kirk both reported higher presence of mono-methylmercury compared to dimethylmercury in the presence of UV light, and with hydroxyl radical's formation under UV light this could be a pathway to the formation of mono-methylmercury. With MeHgOH being such a devastating pollutant due to it high levels of bioaccumulation, it is important understand the production pathways of this contaminant.

These results confirm that dimethylmercury could be a significant source of MeHgOH when they react with the high energy hydroxyl radical. While the current work focused on gas phase reaction, we intend to continue our effort into aqueous phase reactions between organic mercury species such as dimethylmercury and methylmercury and common reactive species such OH and singlet oxygen. This easily leads into the second part of my study investigating the interactions between these highly reactive radicals with the prominent product of this interaction. It can be assumed that if enough hydroxyl radicals are formed it can undergo the second reaction that could lead to the fate

of dimethylmercury in these environments. I hope to inspire more study into the interaction of dimethylmercury with high energy species like the hydroxy radical to uncover possible fates of dimethylmercury in aqueous environments.

Methylmercury Hydroxide Reaction with Hydroxyl Radicals

For the reaction between MeHgOH and hydroxyl radicals, there is six possible reaction channels. Each reaction channels stationary point geometries were optimized with M06-2X, and the geometries are shown below. The single point energies were calculated using CCSD(T) with the AVTZ basis set and the Gibbs free-energy correction was applied at the stationary points to assess the energy barrier for each channel. The Gibbs free-energy profile is shown below with the relative energy barrier for all six possible channels in Figure 4.9.

Table 4.2 includes all the energies and rate constants for all reaction channels using both DFT and CCSD(T) level of theory. The Skodje tunneling approximation was applied to all six channels rate constants. Some channels saw higher contribution to the rate constant due to the higher imaginary frequency of transition state, which allows for a higher chance of tunneling effects to occur. Three of the channels have larger tunneling effects present due to the barrier heights and the imaginary frequencies. The hydrogen abstraction from the methyl group has a large imaginary frequency at 867 cm^{-1} causing an ~50% increase in the reaction rate. The formation of HgOH radical also has a large imaginary frequency (906 cm^{-1}) causing a 170% increase in the reaction rate. The formation of HgOH radical and peroxide has an imaginary frequency of 840 cm-1 causing a 120% increase to the rate constant. The formations of MeHgOH and $Hg(OH)_2$ have small imaginary frequencies (185 cm^{-1} and 134 cm^{-1} respectively) causing only a small increase in the rate constant (<10%). While the hydrogen abstraction from the OH

group has a large imaginary frequency (1254 cm^{-1}), the small energy barrier (<2.5 kcal mol^{-1}) causes the effect to cancel out and only see a 1% increase to the rate constant.

Table 4.2:

Gibbs free energies and rate constants using DFT and CCSD(T) for the six possible reaction channels between MeHgOH and OH

	M062X/DEF2-TVZP		CCSD(T)/AVTZ	
Reaction channel	ΔG[a]	K(TST)[b]	ΔG[a]	K(TST)[b]
•CH_2HgOH[c]	10.2	1.31E-14	4.3	2.98E-10
•$Hg(OH)_2$[d]	12.9	8.61E-17	6.4	4.96E-12
•HgOH+MeOH[e]	24.9	7.51E-25	20.0	1.60E-21
MeHgOH[f]	11.1	1.94E-15	5.8	1.50E-11
•HgOH+H_2O_2[g]	39.9	3.25E-36	36.0	1.99E-33
MeHgO•[h]	7.4	9.04E-13	2.5	3.87E-09

[a] Energy barriers calculated using Gibbs free energy corrections in kcal mol^{-1} [b] k(TST) calculated using transition state theory and Skodje tunneling correction in cm^3 $molecule^{-1}$ s^{-1} [c] Skodje tunneling correction=1.58 [d] Skodje tunneling correction=1.01 [e] Skodje tunneling correction=2.76 [f] Skodje tunneling correction=1.03 [g] Skodje tunneling correction=2.27 [h] Skodje tunneling correction=1.01

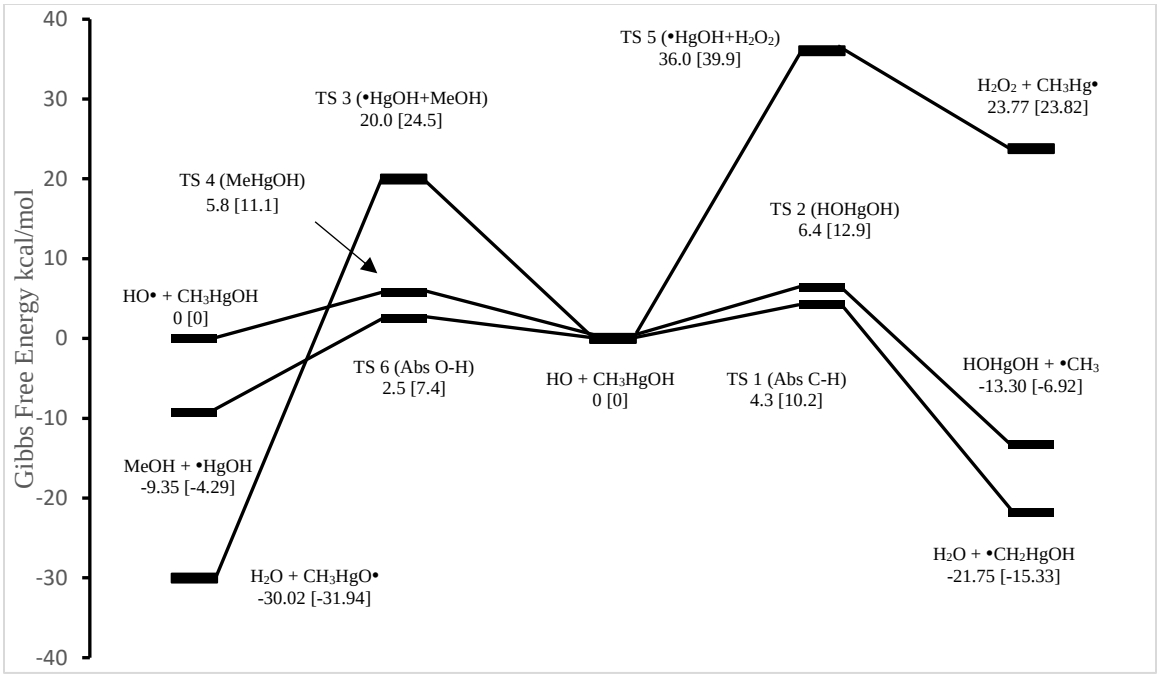

Figure 4.9:
Gibbs free energy profile in kcal mol^{-1} for all possible reaction channels of HO+HOHgMe using CCSD(T)/AVTZ. Values for M06-2X/Def2TZVP are in brackets.

HgOH Radical Formation (Channel 1)

Figures 4.10 and 4.11 describe the optimized geometries for the stationary points and the IRC, respectively, for channel 1. As the hydroxyl radical approached the methyl group, the Hg-C bond length extends as the methyl group is pulled away from the mercury. The initial Hg-C bond length is 2.1 Å, and at the transition state, this bond length extends to 2.3 Å and the O-C bond length is 2.0 Å. The O-Hg-C bond angle stays around 176 degrees. The transition state bond lengths for the HO-C and Hg-C mirror the same reaction channel for dimethylmercury with lengths of 2.3 Å and 2.0 Å, respectively. The hydrogens on the methyl group are pushed more orthogonal to the primary axis of attack and once the methyl group leaves, the hydrogens are pushed further away from the oxygen to form the final product. The final bond length for Hg-O extends from 2.0 Å to 2.1 Å.

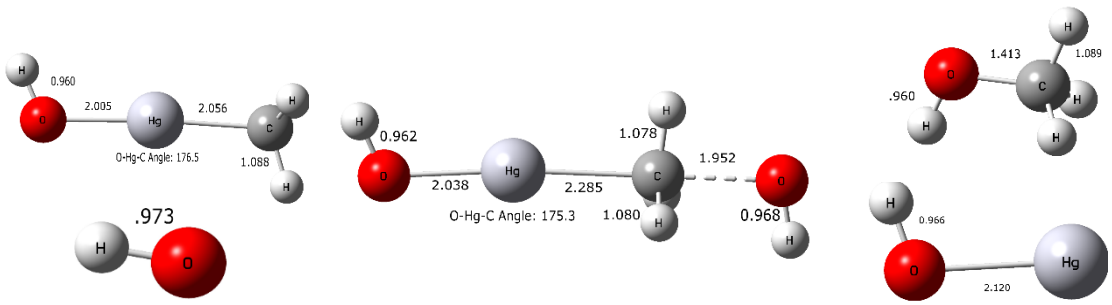

Figure 4.10:
M06-2X optimized geometries for the reactants, products, transition state and pre-reactive complex for channel 1

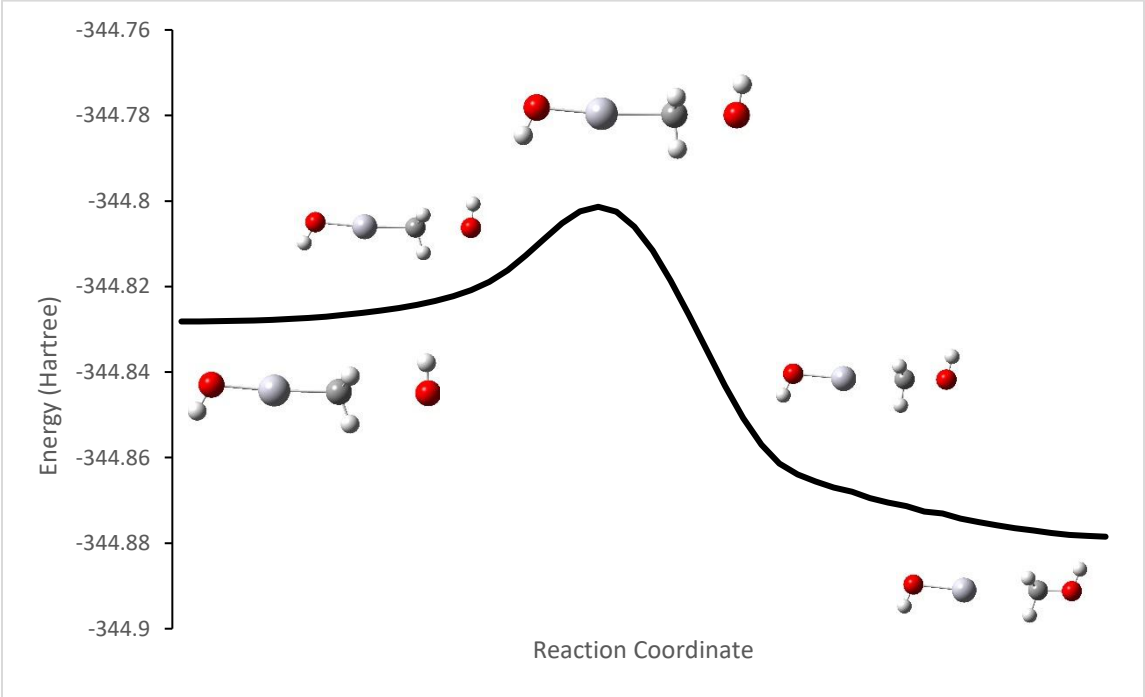

Figure 4.11:
Electronic energies along the minimum energy path for channel 1 starting at the reactants through the products calculated using M06-2X/DEF2-TZVP.

Much like the similar channel studied for dimethylmercury, this channel is the most thermodynamically favorable channel for this interaction. The Gibbs free energy change from reactants to products is -30.0 kcal mol^{-1} for CCSD(T) and -31.9 kcal mol^{-1}

for DFT. While it is the most thermodynamically favored channel for this interaction, it is not kinetically favorable with an energy barrier of 20.0 kcal mol^{-1} for CCSD(T) and 24.5 kcal mol^{-1} for DFT. This high energy barrier makes this channel unlikely to occur at room temperature.

The tunneling correction for this channel is high (~170% increase) due to the large imaginary frequency of 907 cm^{-1}. Applying this correction to the rate constant, the final rate constant is 1.60 x 10^{-21} $molecules^{-1}$ cm^3 for CCSD(T) and 7.51 x 10^{-25} $molcules^{-1}$ cm^3 for DFT. With one of the lowest rate constants among those studied, it is very unlikely this channel has any bearing on the fate of MeHgOH. This is in line with the previously studied dimethylmercury channel that had a rate constant and energy barrier that was too high to have bearing on this interaction.

$Hg(OH)_2$ Formation (Channel 2)

Figures 4.12 and 4.13 describe the optimized geometries for the stationary points and the IRC, respectively, for channel 2. The approach of the hydroxyl radical causes the methyl group to be pushed away from the linear angle and begins to extend the Hg-CH_3 bond. At the transition state, the Hg-C bond length becomes 2.2 Å with an O-Hg-C bond angle of 140.6 degrees. The bond length for the hydroxyl O-Hg is 2.2 Å with an O-Hg-O angle of 138.2 degrees. The bond length is still 1.0 Å longer than the Hg-O bond of the product. This bond length is also 0.2 Å shorter than the O-Hg bond length at the transition state form the similar channel with dimethylmercury. The resulting product $Hg(OH)_2$ has the same bond lengths for both Hg-O bonds with an O-Hg-O bond angle of 180 degrees. It also has an inversion center at the central Hg atom with the hydrogens-oriented opposite to each other. The methyl radical has C-H bond lengths of 1.1 Å and each hydrogen being 120 degrees from each other in a planer orientation.

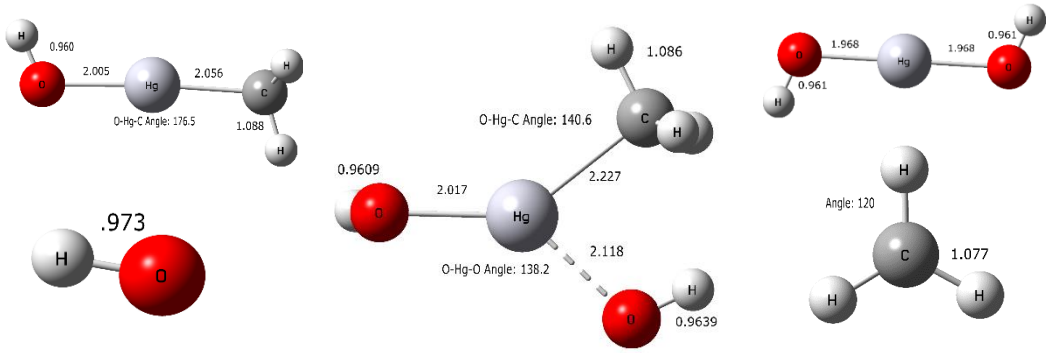

Figure 4.12:
M06-2X optimized geometries for the reactants, products, transition state and pre-reactive complex for channel 2

With an overall Gibbs free energy change of -13.3 kcal mol^{-1} for CCSD(T) and -6.9 kcal mol^{-1} for DFT, this reaction channel is thermodynamically favorable at 298K. This reaction channel is also kinetically favorable with energy barrier of 6.4 kcal mol^{-1} and 12.9 kcal mol^{-1} for CCSD(T) and DFT, respectively. This reaction channel has higher energy barriers than both abstraction reactions, making this channel less likely to occur due to the higher energy barrier. With the energy barrier still below 20.0 kcal mol^{-1}, it can still be expected to occur reasonably at room temperature.

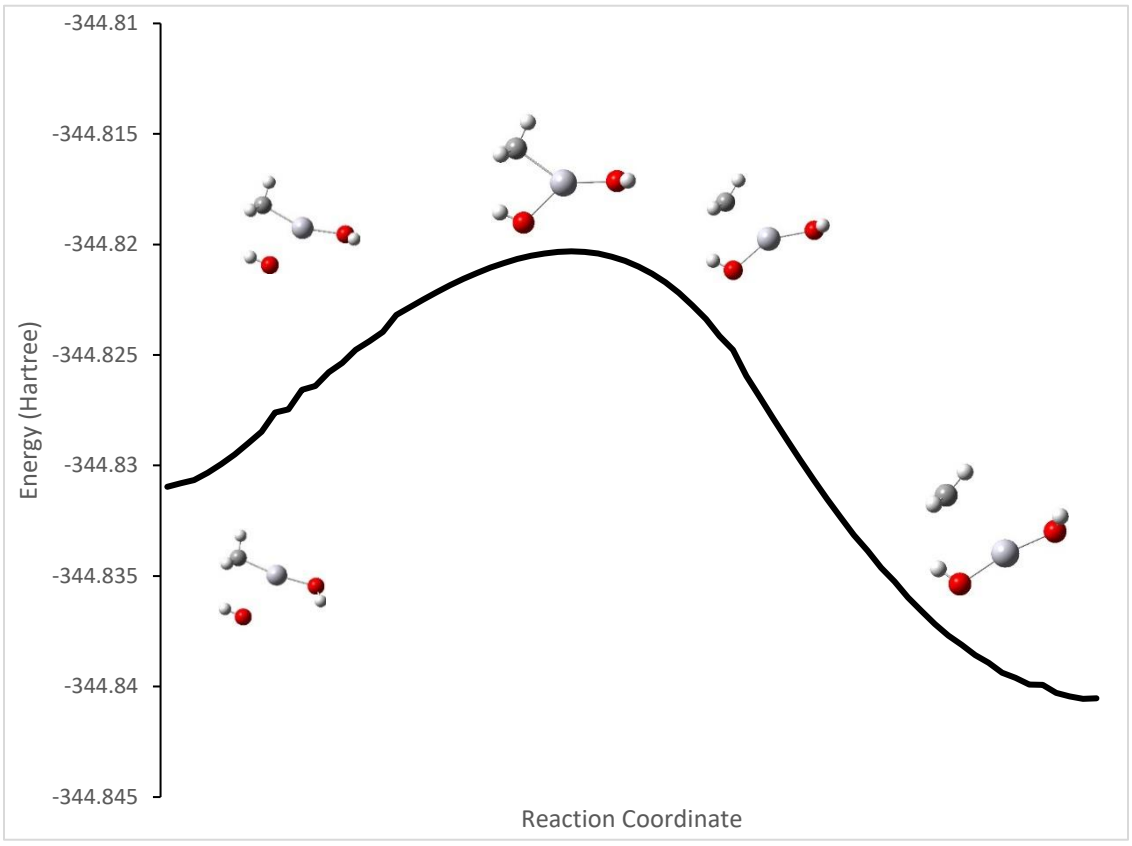

Figure 4.13:
Electronic energies along the minimum energy path for channel 2 starting at the reactants through the products calculated using M06-2X/DEF2-TZVP.

The low imaginary frequency of this channel (134 cm^{-1}) leads to a small Skodje correction factor (~1%). The rate constant for this channel is 4.96 x 10^{-12} $molecules^{-1}$ cm^3 for CCSD(T) and 8.61 x 10^{-17} $molecules^{-1}$ cm^3 for DFT. Unlike with dimethylmercury, the rate constant for this channel is not the fastest among the available channels, making this reaction less likely to occur when compared to other channels.

Hydrogen Abstraction from CH_3 (Channel 3)

Figures 4.14 and 4.15 show the optimized geometries for the stationary points along the reaction coordinate and the IRC, respectively, for the hydrogen abstraction channel. Much like the abstraction channel found with dimethylmercury, the approach of the hydroxyl radical causes an elongation of the C-H bond in question. At the optimal transition state, the C-H bond length is 1.2 Å, and the O-H bond length is 1.4 Å. This corresponds well with the abstraction from methane, which has C-H and O-H bond lengths of 1.2 Å and 1.3 Å, respectively. This also corresponds well with the dimethylmercury abstraction channel which the same bond lengths for C-H and O-H. This result is expected as the hydroxy group on the mercury has little interaction with the incoming hydroxyl radical due to the distance between them being 4.0 Å. The length of the Hg-OH bond has no change at the transition state, and the O-Hg-C bond angle stays the same over the course of the reaction. After the abstraction has occurred, the Hg-C bond length shortens from 2.1 Å to 2.0 Å.

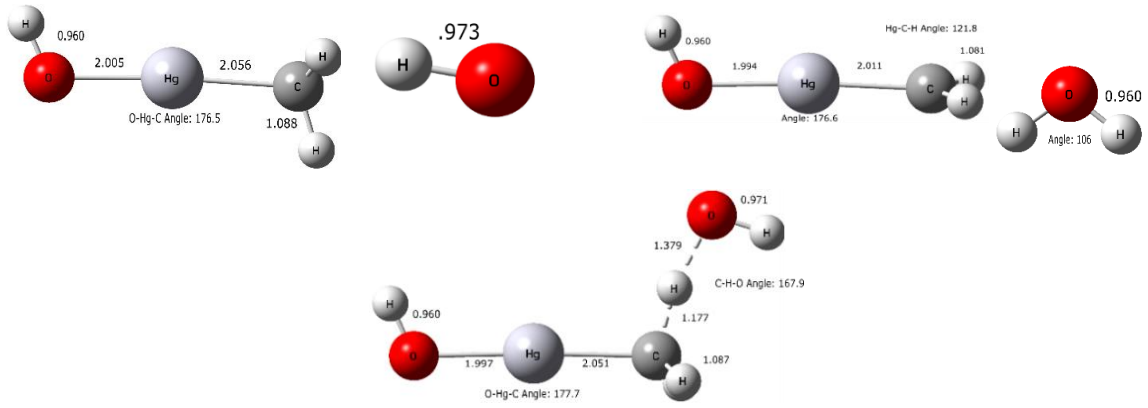

Figure 4.14:
M06-2X optimized geometries for the reactants, products, transition state and pre-reactive complex for channel 3

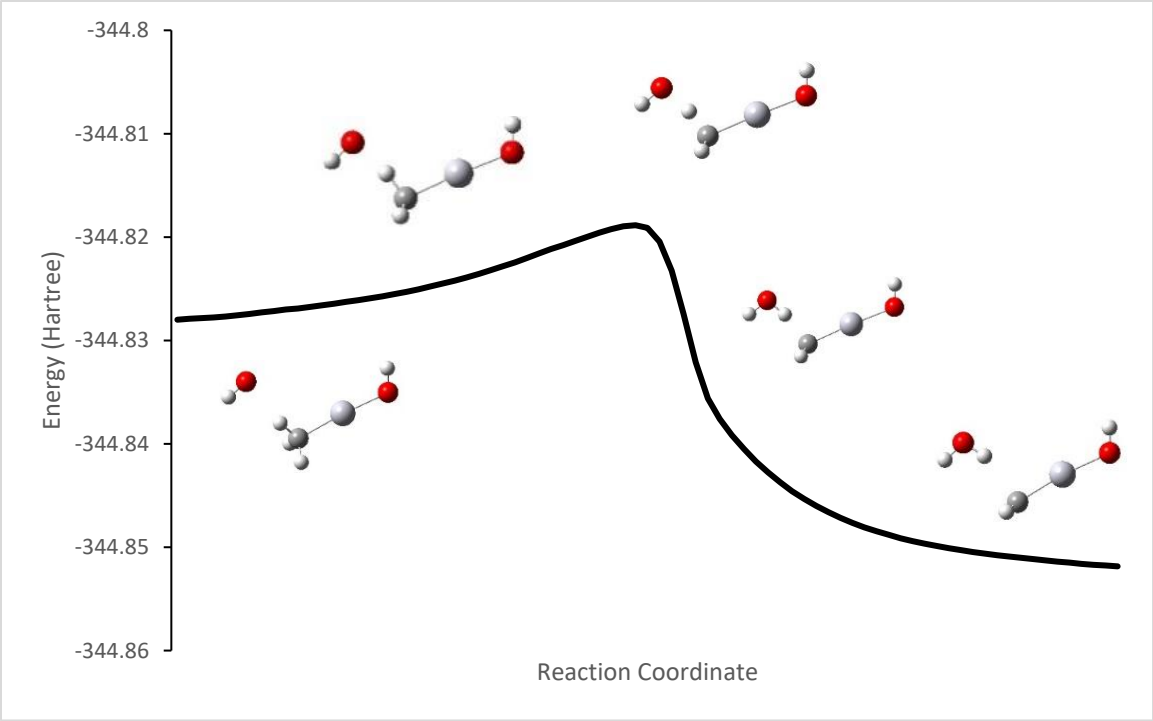

Figure 4.15:
Electronic energies along the minimum energy path for channel 3 starting at the reactants through the products calculated using M06-2X/DEF2-TZVP

This reaction channel is highly exergonic at 298 K with a Gibbs free energy change of -21.8 kcal mol^{-1} for CCSD(T) and -15.3 kcal mol^{-1} for M06-2X. This reaction is thermodynamically favorable at room temperature and the products can be expected to be stable under these conditions. The methyl radical is stabilized by the mercury it is attached to and the hydroxy radical becomes stabilized as water. This leads to lower energy products that are far more stable than the initial reactants. This reaction channel is also kinetically favorable with an energy barrier of 4.2 kcal mol^{-1} for CCSD(T) and 10.2 kcal mol^{-1} for M06-2X.

Much like previously studied abstraction reaction channels, this channel has a significant tunneling effect occur that increased the rate constant at 298K. With a large imaginary frequency of 867 cm^{-1} the tunneling correction has a 50% increase in the overall rate constant for the reaction. The rate constant at 298 K for the hydrogen abstraction channel is 2.98 x 10^{-10} $molecules^{-1}$ cm^3 for CCSD(T) and 1.31 x 10^{-14} for DFT. The CCSD(T) calculated rate constant is orders of magnitude faster than the rate constant calculated for the same channel due to the lower energy barrier calculated by CCSD(T). Unlike with dimethylmercury, this reaction channel is faster than the reaction channel that replaces the methyl group and be expected to occur with a higher probably over the formation of $Hg(OH)_2$.

Hydrogen Abstraction from OH (Channel 4)

Figures 4.16 and 4.17 describe the optimized geometries for the stationary points and the IRC, respectively, for the abstraction channel. As expected, upon approach of the hydroxyl radical, the O-H bond extends as the hydrogen begins to interact with the radical. At the transition state, the O-H bond of MeHgOH is at 1.1 Å and the HO-H bond is 1.3 Å. Much like the previous abstraction reactions studied, the Hg-C bond has no change in length but there is a 2-degree change in the O-Hg-CH_3 bond angle. The HO-H

bond length matches well to the other studied bond lengths for this interaction. Unlike other abstraction channels, the hydrogen of the hydroxyl radical is not oriented planar to the rest of the molecule, but rather is orthogonal to the molecule, likely due to the coulombic interactions. Due to the electronegativity of the oxygen, hydrogen will coordinate to the oxygen of MeHgOH while trying to minimize the partial positive H-H interaction.

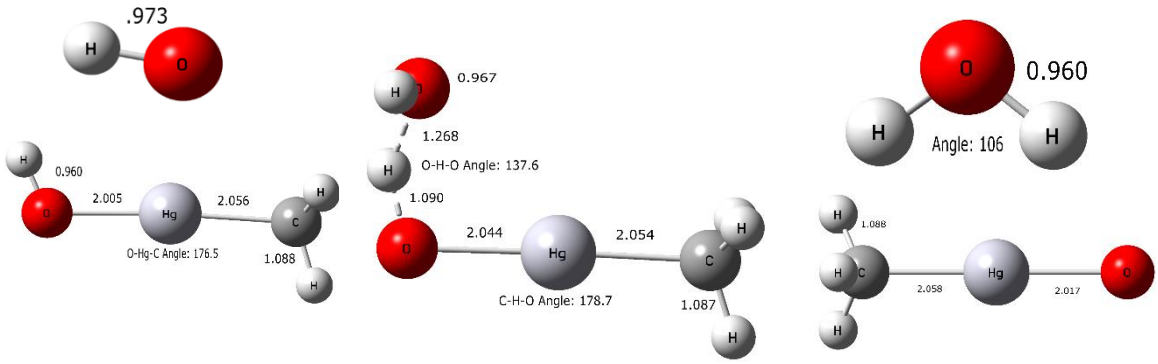

Figure 4.16:
M06-2X optimized geometries for the reactants, products, transition state and pre-reactive complex for channel 4

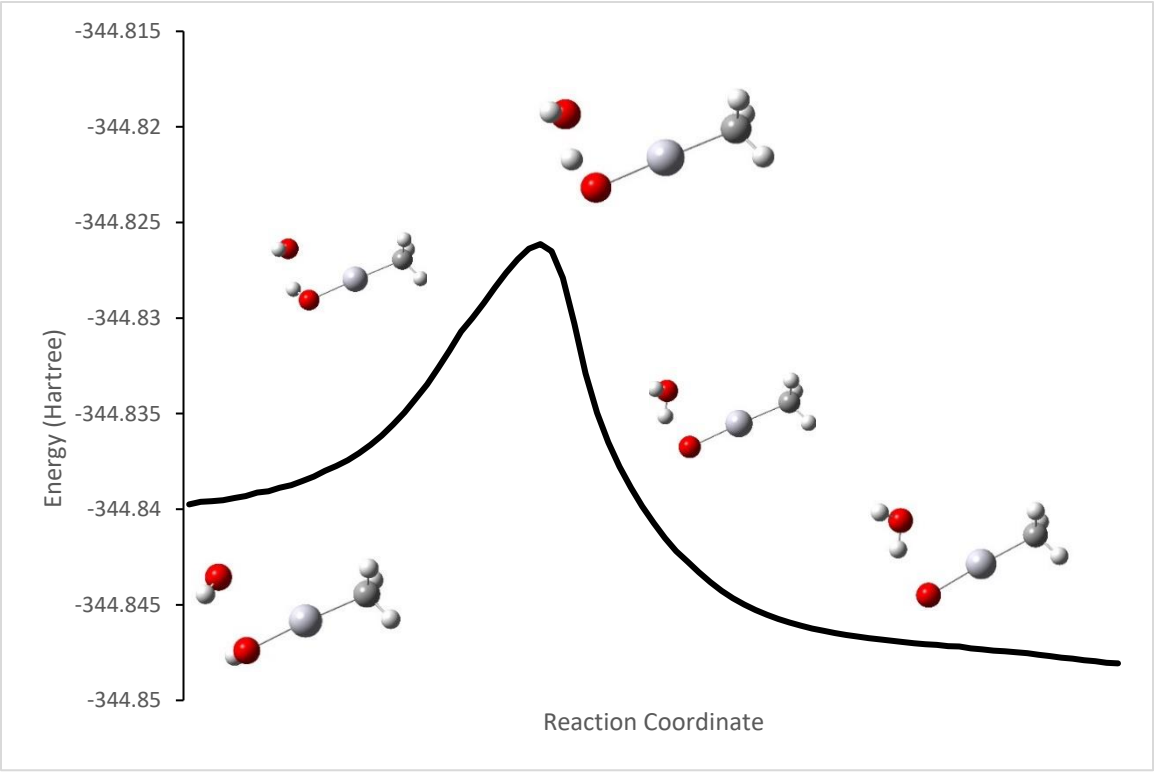

Figure 4.17:
Electronic energies along the minimum energy path for channel 4 starting at the reactants through the products calculated using M06-2X/DEF2-TZVP.

This reaction channel is exergonic with an overall Gibbs free energy change of -9.4 kcal mol^{-1} for CCSD(T) and -4.3 kcal mol^{-1} for DFT. With this energy change being negative, the reaction is thermodynamically favorable at 298 K and can be expected to occur. The final oxygen radical is stabilized by both the electronegativity of oxygen and the attachment of oxygen to mercury. This channel is also kinetically favorable with and energy barrier of 2.5 kcal mol^{-1} for CCSD(T) and 7.4 kcal mol^{-1} for DFT.

While this reaction has a large imaginary frequency even at room temperature (1254 cm^{-1}), the low energy barrier at 2.5 kcal mol^{-1} negates the imaginary frequency and makes it less likely for tunneling to occur using the Skodje approximation. The final rate constant calculated from the CCSD(T) Gibbs free energy is 3.87 x 10^{-9}

molecule^{-1} cm^3 (9.04 x 10^{-13} molecules^{-1} cm^3 for DFT). This rate constant is the fastest among all the channels studied for this reaction, making it the most kinetically favorable channel. This makes this channel the most likely channel to dominate this interaction.

•HgMe and Peroxide Formation (Channel 5)

Figures 4.18 and 4.19 describe the optimized geometries for the stationary points and the IRC, respectively, for channel 5. As the hydroxyl radical approaches, the OH group is pulled away from the mercury atom and the bond angle begins to deviate from linearity. At the transition state, the O-Hg bond length extends to 2.4 Å with an O-Hg-C bond angle of 163.5 degrees. The Hg-CH_3 bond length extends to 2.2 Å and extends further after the OH group leaves. The O-O bond length shortens to 1.6 Å and the O-O-Hg angle is 163.8 degrees. The hydrogens on each oxygen begin to orient to each other, with a H-O-O-H dihedral angle of 119.0 degrees. As the peroxide group leaves, the hydrogens of the peroxide molecule orient 180 degrees from each other with a final O-O bond length of 1.4 Å. The final Hg-C bond length for MeHg is 2.3 Å.

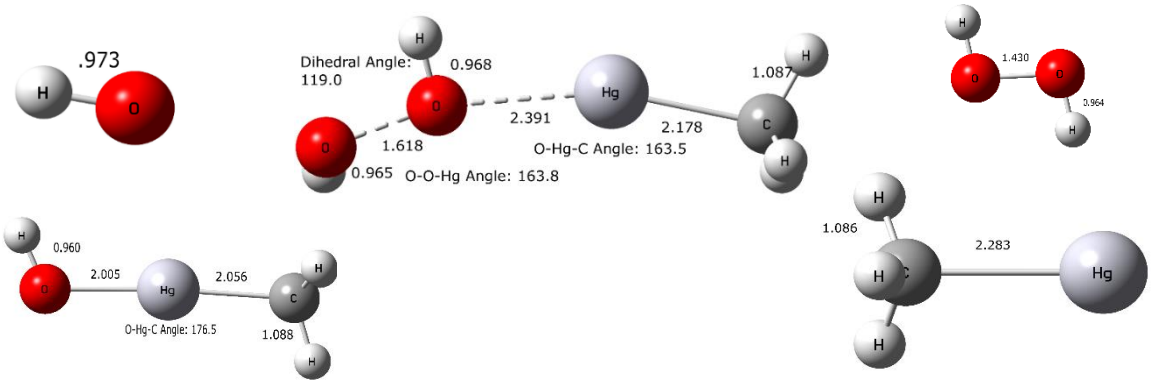

Figure 4.18:
M06-2X optimized geometries for the reactants, products, transition state and pre-reactive complex for channel 5

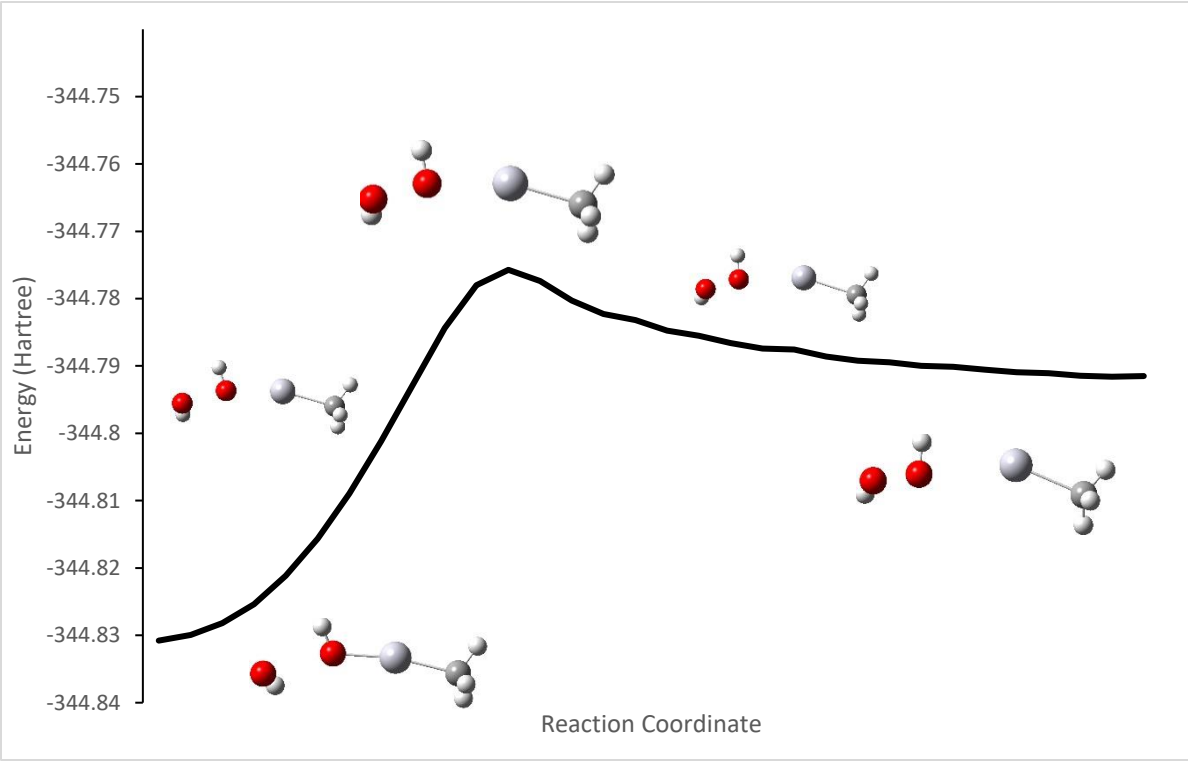

Figure 4.19:
Electronic energies along the minimum energy path for channel 5 starting at the reactants through the products calculated using M06-2X/DEF2-TZVP

Unlike the other channels seen in this reaction, this interaction is thermodynamically unfavored to the high energy difference between the reactants and products. The energy difference seen is 23.8 kcal mol^{-1} for CCSD(T) and DFT. This channel is also kinetically unfavored with an energy barrier of 36.1 kcal mol^{-1} for CCSD(T) and 39.9 kcal mol^{-1} for DFT. With the reactants being more favored over the products, even if there is sufficient energy to overcome the energy barrier, it is likely the transition state will still move back to MeHgOH + ·OH rather than form the products.

This lack of favorability is also seen in the rate constant. Even with the large tunneling correction (120% due to the large imaginary frequency of 840 cm^{-1}), the rate constant is the lowest by many orders of magnitude. After application of the tunneling correction, the rate constant for this channel is 1.99 x 10^{-33} $molecules^{-1}$ cm^3 for CCSD(T)

and 3.25 x 10^{-36} molecules^{-1} cm^3 for DFT. With this small rate constant, there is little chance of this reaction occurring at room temperature and thus this channel will have little bearing on the fate of MeHgOH.

Reformation of MeHgOH (Channel 6)

Figures 5.8 and 5.9 describe the optimized geometries for the stationary points and the IRC, respectively, for channel 6. This reaction channel is a possible pathway that can lead to the reformation of MeHgOH and can be thought of as an equilibrium reaction. There is no disappearance of the reactants as they are reformed through this process but since it is still a possible channel it has been characterized. At the transition state, the bond lengths for O-Hg on both hydroxyl groups are 2.2 Å and they both have the same O-Hg-C angle of 150.7 degrees. This similarity is expected as both hydroxyl radicals are the same, leading to the same interaction occurring between the O-Hg for each. The hydrogens of each hydroxyl group are on the same side of the molecule with the same O-H bond length of 1.0 Å. Compared to the products/reactants, the Hg-O bond lengths are 0.2 Å longer. The IRC for the reaction is a bell curve with the reactants and products energies being equal as expected.

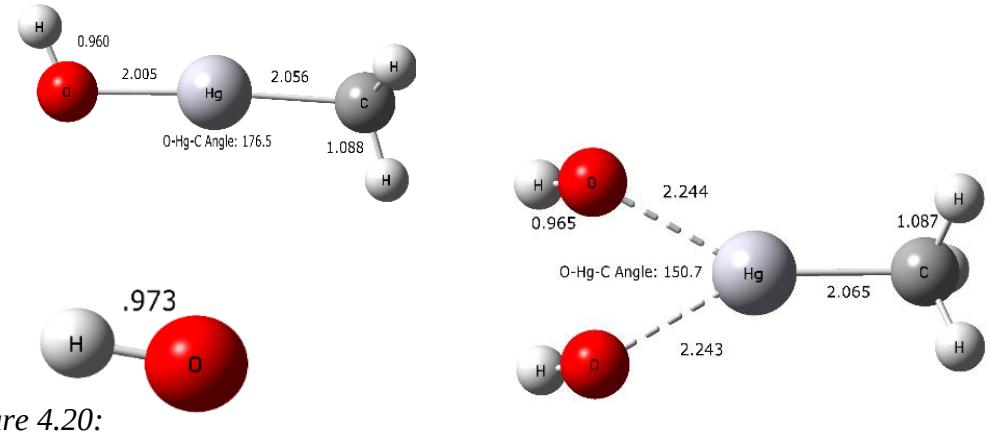

Figure 4.20:
M06-2X optimized geometries for the reactants, products, transition state and pre-reactive complex for channel 6.

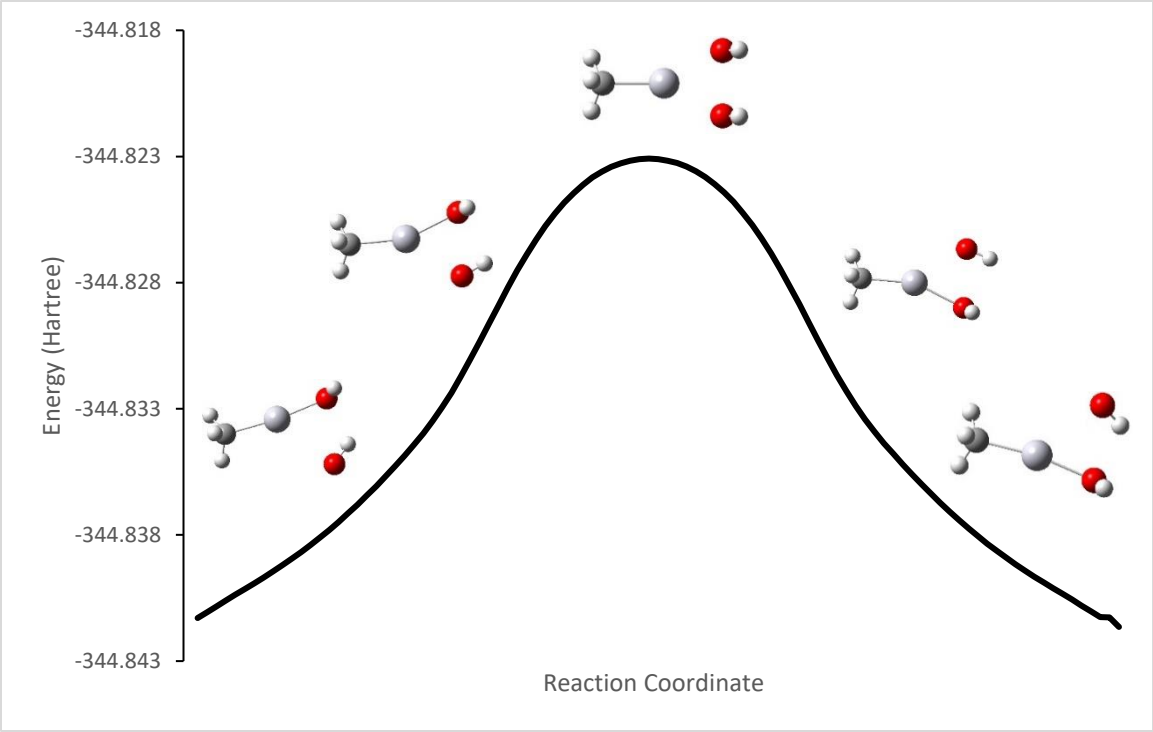

Figure 4.21:
Electronic energies along the minimum energy path for channel 6 starting at the reactants through the products calculated using M06-2X/DEF2-TZVP.

As this reaction is a re-formation of the products, this channel can be considered as an equilibrium reaction which has no overall change in the Gibbs free energy of the reactants and the products. The energy barrier for this channel is 5.8 kcal mol^{-1} for CCSD(T) and 11.1 kcal mol^{-1} for DFT. This low energy barrier makes this interaction kinetically favorable at room temperature, but since there is no change in the products formed by this interaction, it is not expected to contribute to the overall fate of MeHgOH. Had the barrier been lower than other channels, it could be possible to conclude that MeHgOH would likely be the final product of this interaction, which is not the case. Other channels, notably the abstraction channels, have lower energy barriers making them more kinetically favorable over this channel.

The tunneling correction for this channel is low (~3%) due to the low imaginary frequency at 185 cm^{-1}. The overall rate constant for this channel is 1.50 x 10^{-11}

molecules^{-1} cm^3 for CCSD(T) and 1.94 x 10^{-15} molecules^{-1} cm^3 for DFT. This rate constant can be thought of as the equilibrium rate constant K_{eq}. With this rate constant being lower than other channels, this interaction can be expected to occur at 298 K but will be not make a significant contribution to the fate of MeHgOH. While this result was expected, it was important to verify this conclusion before concluding other channels will dominate over this channel.

Discussion

All thermodynamically possible reaction channels were studied with *ab-initio* methods with various channels being more kinetically or thermodynamically accessible than others. There is little to no experimental data to the author's knowledge on this interaction, thus the energy barriers and rate constants cannot be compared to empirical evidence. All further discussion of the results can only be based on the calculated rate energy from Gaussian.

The formation of MeHg radical and peroxide was both thermodynamically unfavorable due to higher energy products being formed and kinetically unfavorable since the energy barrier is extremely high. Based on this conclusion, it is highly unlikely that this reaction channel has significant bearing on the fate of MeHgOH. This could be attributed to the far higher energy product peroxide, which is highly reactive due to instability. Peroxide is highly reactive, and the O-O bond will readily dissociate into O_2 and H_2O, which if this channel could occur peroxide would likely undergo this final transformation. However, since the energy barrier is well over 20 kcal mol^{-1}, it is unlikely to be a product of this interaction. The formation of ·HgOH and MeOH, while thermodynamically accessible is unlikely to occur since the energy barrier is nearly 20 kcal mol^{-1}. At room temperature, this channel is kinetically unfavorable and will likely not occur. This observation is in line with the similar channel studied for

dimethylmercury that was also kinetically unfavorable. Niki et al.[9] observed that this channel did not occur with dimethylmercury and while the reactants are slightly different, it falls in line that this channel will be unlikely to occur. The equilibrium channel is thermodynamically neutral as the reactants and the products for this channel are the same. It is kinetically favorable at room temperature but even if this reaction channel does occur, there is no change overall to the amount of MeHgOH present, and thus the products of this channel can further react through other channels. Had this channel been the most kinetically favorable, it could be assumed that other channels would be less likely to occur making the degradation of MeHgOH rate constant take longer. Since this is not the case, it can be assumed that other channels will predominate and allow MeHgOH to degrade.

While the replacement of the methyl group by the hydroxyl radical is the most kinetically favored with dimethylmercury, the same channel is not the most kinetically favored with methylmercury hydroxide. The reaction channel is both kinetically and thermodynamically favorable, with a low energy barrier, but it is not the lowest energy barrier of the six possible channels. It can be expected based on the energy barrier difference that mercury hydroxide is not a likely product for this interaction. Both hydrogen abstraction reactions (from the ·OH and ·CH_3) are thermodynamically and kinetically favorable. The hydrogen abstraction from the -CH_3 has a low energy barrier (4 kcal mol^{-1}) thus is likely to occur at room temperature depending on the side of the attack of the hydroxyl radical. The hydrogen abstraction from the -OH is thermodynamically favorable and the most kinetically favorable of all the studied channels. This makes MeHgO radical the most likely product of this interaction. Since the ·CH_2HgOH channel is only 2 kcal mol^{-1} higher than the MeHgO· channel, it can be expected that both will be plausible products, with MeHgO· being the dominating product. While the $Hg(OH)_2$

channel has a low energy barrier (~6 kcal mol^{-1}), with it being nearly 4 kcal mol^{-1} higher than the dominate channel, it can be assumed based on the theoretical data that $Hg(OH)_2$ is not a likely product formed at room temperature.

CHAPTER V:

CONCLUSION

Reactions

After analysis of the rate constants and Gibbs free energies of each reaction channel for dimethylmercury and hydroxyl radicals, it was found that the primary product of this interaction should be methylmercury hydroxide. Due to the 4 kcal mol^{-1} difference, it can be expected that most of the interactions yield MeHgOH with a minor amount undergoing the abstraction channel. While this interaction was studied in the gas phase, it can be expected that these interactions will have similar pathways in the aqueous phase. As hydroxyl radicals can readily be formed in ocean water and the atmosphere, it is possible that these high energy species interact with dimethylmercury, and cause demethylation to occur. This process will form MeHgOH, which can further react with available hydroxyl radicals. While demethylation would also include the formation of MeHg• and methanol, due to the high energy barrier it is not likely that this is a plausible pathway for demethylation. This result correlates with the empirical study for this interaction by Niki et al.[9], with the expectation that methylmercury hydroxide is the primary product of this interaction.

For the interaction of methylmercury hydroxide with hydroxyl radicals, there are six possible channels. Three of these channels are kinetically favorable at room temperature, being both the hydrogen abstraction channels and the demethylation channel to form $Hg(OH)_2$. While the demethylation channel is possible at room temperature, due to the higher energy relative to both abstraction channels, it is unlikely that $Hg(OH)_2$ will be formed in considerable quantities. The hydrogen abstraction channel in which the hydrogen comes from the OH group on methylmercury hydroxide has the lowest energy barrier of all the reaction channels. Based on the results, the dominant product of this

reaction will be MeHgO radical with a possible but minimal side product being CH_2HgOH radical.

Organic Mercury Fate

The purpose of my thesis was to determine the role that hydroxyl radicals play in the overall fate of organic mercury in the environment. While my study considered reactions in the gas phase with no solvent effects present, it is a good starting point and will provide the base to construct a theoretical model on the fate of organic mercury.

As mercury is released into the atmosphere from different sources, such as coal mining and powerplants, it will be carried through the air to different areas. In the atmosphere, different chemical reactions will occur, such as those proposed by Dibble and others[5,12,21,27-29], that will form inorganic mercury. These various forms of inorganic mercury will then deposit from the atmosphere into both the land and aquatic environments. Once the inorganic mercury has been deposited into these environments, bacteria, such as *Desulfovibrio desulfuricans*, can convert inorganic mercury to organic mercury species like dimethylmercury. Any organic mercury that is in the soil near waterways will transfer into the water and join the other organic mercury species present. Evidence has shown[10,33,34] that dimethylmercury has a lower probability of being converted to mono-methylmercury without the presence of sunlight. This means at the lower depths of the ocean dimethylmercury will be the predominant form of organic mercury. As dimethylmercury starts to propagate up to the higher levels of the ocean, more light is present to induce the demethylation of dimethylmercury. Based on the results of my theoretical study, it is possible that the reaction with hydroxyl radicals can lead to demethylation of dimethylmercury. The first interaction of hydroxyl radicals with dimethylmercury will likely create methylmercury hydroxide as the primary product. Assuming there is an abundance of hydroxyl radicals present, a second interaction can

occur between these species. Unlike the first interaction, it is highly unlikely that the hydroxyl radical will further demethylate MeHgOH, instead the most likely interaction is a hydrogen abstraction to create MeHgO· radical. This theory matches well with the data present on the concentrations of both forms of methylated mercury in different depths of water. In deeper waters without the presence of sunlight to radicalize water, little methylmercury hydroxide is present since there is no pathway to demethylation. In more shallow water, where sunlight is available to create a hydroxyl radical, more methylmercury hydroxide is formed.

Further Works

All the geometries, energies and rate constants were calculated in the gas phase only. While this is a reasonable prediction based on the resources available, this energy can be better corrected to fit the environmental conditions that need to be studied. Optimally, the next step in this research is to study these interactions with solvent effects included as the extra interactions formed by the solvents will cause changes in energy and possibly changes in the optimized geometries. While I believe this is a great starting point, to fully understand the mercury chain these reactions must be studied in the solution phase.

Another topic that should be studied further is different high energy species of radicals that can be found in oceanic conditions. The reaction of chlorine radicals with dimethylmercury is currently being investigated by another member of the lab. Another reaction that should be investigated is the reaction of a chlorine radical with methylmercury hydroxide. Both studies are analogous to the reactions that I have studied and are a good extension to further understand the mercury chain. While not presented here, I have begun to study the interaction of methylmercury chloride with a hydroxyl radical. All further research will provide a better picture of the mercury chain in the

environment, especially since methylmercury chloride is a major form of mono-methylmercury.

REFERENCES

1. Han, F. X.; Banin, A.; Su, Y.; Monts, D. L.; Plodinec, J. M.; Kingery, W. L.; Triplett, G. E. Industrial Age Anthropogenic Inputs of Heavy Metals into the Pedosphere. *Naturwissenschaften* **2002**, *89* (11), 497–504.
2. Raskin, I.; Ensley, B. D. *Phytoremediation of toxic metals: using plants to clean up the environment*; Lightning Source UK Ltd.: Milton Keynes, UK, **2011**.
3. Gilmour, C. C.; Riedel, G. S.; Riedel, G.; Kwon, S.; Landis, R.; Brown, S. S.; Menzie, C. A.; Ghosh, U. Activated Carbon Mitigates Mercury and Methylmercury Bioavailability in Contaminated Sediments. *Environmental Science & Technology* **2013**, *47* (22), 13001–13010.
4. Tsuda, T.; Yorifuji, T. The History of Minamata Disease and Public Health Policy. *Epidemiology* **2011**, *22*.
5. Fitzgerald, W. F.; Lamborg, C. H.; Hammerschmidt, C. R. Marine Biogeochemical Cycling of Mercury. https://pubs.acs.org/doi/10.1021/cr050353m (accessed May 17, 2021).
6. Jonsson, S.; Mazrui, N. M.; Mason, R. P. Dimethylmercury Formation Mediated by Inorganic and Organic Reduced Sulfur Surfaces. *Scientific Reports* **2016**, *6* (1).
7. Baya, P. A.; Gosselin, M.; Lehnherr, I.; St.Louis, V. L.; Hintelmann, H. Determination of Monomethylmercury and Dimethylmercury in the Arctic Marine Boundary Layer. *Environmental Science & Technology* **2014**, *49* (1), 223–232.
8. Bytautas, L. Stability of Dimethylmercury and Related Mercury-Containing Compounds with Respect to Selected Chemical Species Found in Aqueous Environment. *Croatica Chemica Acta* **2013**, *86* (4), 453–462.
9. Niki, H.; Maker, P. D.; Savage, C. M.; Breitenbach, L. P. A Long-Path Fourier Transform Infrared Study of the Kinetics and Mechanism for the Hydroxyl

Radical-Initiated Oxidation of Dimethylmercury. *The Journal of Physical Chemistry* **1983**, *87* (24), 4978–4981.

10. Morel, F. M.; Kraepiel, A. M.; Amyot, M. THE CHEMICAL CYCLE AND BIOACCUMULATION OF MERCURY. *Annual Review of Ecology and Systematics* **1998**, *29* (1), 543–566.
11. Tossell, J. A. Theoretical Study of the Photodecomposition of Methyl Hg Complexes. *The Journal of Physical Chemistry A* **1998**, *102* (20), 3587–3591.
12. Gworek, B.; Bemowska-Kałabun, O.; Kijeńska, M.; Wrzosek-Jakubowska, J. Mercury in Marine and Oceanic Waters—a Review. *Water, Air, & Soil Pollution* **2016**, *227* (10).
13. Bradley, M.; Barst, B.; Basu, N. A Review of Mercury Bioavailability in Humans and Fish. *International Journal of Environmental Research and Public Health* **2017**, *14* (2), 169.
14. Hong, Y.-S.; Kim, Y.-M.; Lee, K.-E. Methylmercury Exposure and Health Effects. *Journal of Preventive Medicine & Public Health* **2012**, *45* (6), 353–363.
15. Niki, H.; Maker, P. S.; Savage, C. M.; Breitenbach, L. P. A Fourier-Transform Infrared Study of the Kinetics and Mechanism of the Reaction of Atomic Chlorine with Dimethylmercury. *The Journal of Physical Chemistry* **1983**, *87* (19), 3722–3724.
16. Goldman, L. R.; Shannon, M. W. Technical Report: Mercury in the Environment: Implications for Pediatricians. *PEDIATRICS* **2001**, *108* (1), 197–205.
17. Pehkonen, S. O.; Lin, C.-J. Aqueous Photochemistry of Mercury with Organic Acids. *Journal of the Air & Waste Management Association* **1998**, *48* (2), 144–150.
18. Selin, N. E. Global Biogeochemical Cycling of Mercury: A Review. *Annual Review of Environment and Resources* **2009**, *34* (1), 43–63.

19. Jacobs, L. W.; Keeney, D. R. Methylmercury Formation in Mercury-Treated River Sediments During in Situ Equilibration. *Journal of Environmental Quality* **1974**, *3* (2), 121–126.

20. JENSEN, S.; JERNELÖV, A. Biological Methylation of Mercury in Aquatic Organisms. *Nature* **1969**, *223* (5207), 753–754.

21. Baldi, F.; Pepi, M.; Filippelli, M. Methylmercury Resistance in Desulfovibrio Desulfuricans Strains in Relation to Methylmercury Degradation. *Applied and Environmental Microbiology* **1993**, *59* (8), 2479–2485.

22. CRAIG, P. J.; BARTLETT, P. D. The Role of Hydrogen Sulphide in Environmental Transport of Mercury. *Nature* **1978**, *275* (5681), 635–637.

23. Asaduzzaman, A. M.; Schreckenbach, G. Degradation Mechanism of Methylmercury Selenoamino Acid Complexes: A Computational Study. *Inorganic Chemistry* **2011**, *50* (6), 2366–2372.

24. Rahmanikhah, Z.; Esmaili-sari, A.; Bahramifar, N. Total Mercury and Methylmercury Concentrations in Native and Invasive Fish Species in Shadegan International Wetland, Iran, and Health Risk Assessment. *Environmental Science and Pollution Research* **2020**, *27* (7), 6765–6773.

25. Karita, K.; Iwata, T.; Maeda, E.; Sakamoto, M.; Murata, K. Assessment of Cardiac Autonomic Function in Relation to Methylmercury Neurotoxicity. *Toxics* **2018**, *6* (3), 38.

26. Choi, A. L.; Grandjean, P. Methylmercury Exposure and Health Effects in Humans. *Environmental Chemistry* **2008**, *5* (2), 112.

27. Dibble, T. S.; Zelie, M. J.; Mao, H. Thermodynamics of Reactions of ClHg and BrHg Radicals with Atmospherically Abundant Free Radicals. *Atmospheric Chemistry and Physics* **2012**, *12* (21), 10271–10279.

28. Lam, K. T.; Wilhelmsen, C. J.; Dibble, T. S. BrHgO• + C2H4 and BrHgO• + HCHO in Atmospheric Oxidation of Mercury: Determining Rate Constants of Reactions with Pre-Reactive Complexes and a Bifurcation. *J. Phys. Chem. A* **2019**, *123*, 6045–6055.

29. Lam, K. T.; Wilhelmsen, C. J.; Schwid, A. C.; Jiao, Y.; Dibble, T. S. Computational Study on the Photolysis of BrHgONO and the Reactions of BrHgO• with CH_4, C_2H_6, NO, and NO_2: Implications for Formation of Hg(II) Compounds in the Atmosphere. *The Journal of Physical Chemistry A* **2019**, *123* (8), 1637–1647.

30. Castro, L.; Dommergue, A.; Larose, C.; Ferrari, C.; Maron, L. A Theoretical Study of Abiotic Methylation Reactions of Gaseous Elemental Mercury by Halogen Containing Molecules. **2010**.

31. Shagun, V. A.; Shevchenko, S. G.; Smirnov, V. I.; Frolov, Y. L. Quantum Chemical Study of Complexation Effects of Monomethylmercury Cation with Inorganic Ligands (Cl, Br, I, HO, HS, HSe) in Aqueous Medium. *Journal of Structural Chemistry* **2005**, *46* (2), 230–236.

32. Lee, E. P. F.; Wright, T. G. Thermochemistry of $HgCH_3$ and $HgCH_3$+ and the Ionization Energy of $HgCH_3$. *Chemical Physics Letters* **2003**, *376* (3-4), 418–423.

33. Kirk, J. L. Potential Sources of Monomethylmercury in Arctic and Subarctic Seawater. *ARCTIC* **2009**, *59* (1).

34. Pan, S.; Feng, C.; Lin, J.; Cheng, L.; Wang, C.; Zuo, Y. Occurrence and Photodegradation of Methylmercury in Surface Water of Wen-Rui-Tang River Network, Wenzhou, China. *Environmental Science and Pollution Research* **2017**, *24* (12), 11289–11298.

35. Chen, J.; Pehkonen, S. O.; Lin, C.-J. Degradation of Monomethylmercury Chloride by Hydroxyl Radicals in Simulated Natural Waters. *Water Research* **2003**, *37* (10), 2496–2504.

36. GaussView, Version 5, Dennington, Roy; Keith, Todd A.; Millam, John M. Semichem Inc., Shawnee Mission, KS, **2009**.

37. Gaussian 16, Revision C.01, Frisch, M. J.; Trucks, G. W.; Schlegel, H. B.; Scuseria, G. E.; Robb, M. A.; Cheeseman, J. R.; Scalmani, G.; Barone, V.; Petersson, G. A.; Nakatsuji, H.; et al. Gaussian, Inc., Wallingford CT, **2016**.

38. Gaussian 09, Revision D.01, Frisch, M. J.; Trucks, G. W.; Schlegel, H. B.; Scuseria, G. E.; Robb, M. A.; Cheeseman, J. R.; Scalmani, G.; Barone, V.; Petersson, G. A.; Nakatsuji,; et al. Gaussian, Inc., Wallingford CT, **2016**.

39. Weigend, F.; Ahlrichs, R. Balanced Basis Sets of Split Valence, Triple Zeta Valence and Quadruple Zeta Valence Quality for H to Rn: Design and Assessment of Accuracy. *Physical Chemistry Chemical Physics* **2005**, *7* (18), 3297.

40. Weaver, M. N.; Merz, K. M. Assessment of the CCSD and CCSD(T) Coupled-Cluster Methods in Calculating Heats of Formation for Cu Complexes. *Molecular Physics* **2009**, *107* (8-12), 1251–1259.

41. Zhao, Y.; Truhlar, D. G. The M06 Suite of Density Functionals for Main Group Thermochemistry, Thermochemical Kinetics, Noncovalent Interactions, Excited States, and Transition Elements: Two New Functionals and Systematic Testing of Four M06 Functionals and 12 Other Functionals. *Theoretical Chemistry Accounts* **2008**, *119* (5-6), 525–525.

42. Dunning, T. H. Gaussian Basis Sets for Use in Correlated Molecular Calculations. I. The Atoms Boron through Neon and Hydrogen. J. Chem. Phys. **1989**, 90 (2), 1007−1023.

43. Kendall, R. A.; Dunning, T. H.; Harrison, R. J. Electron Affinities of the First-row Atoms Revisited. Systematic Basis Sets and Wave Functions. J. Chem. Phys. **1992**, 96 (9), 6796−6806.

44. Peterson, K. A.; Puzzarini, C. Systematically Convergent Basis Sets for Transition Metals. II. Pseudopotential-Based Correlation Consistent Basis Sets for the Group 11 (Cu, Ag, Au) and 12 (Zn, Cd, Hg) Elements. Theor. Chem. Acc. **2005**, 114 (4−5), 283−296.

45. Skodje, R. T.; Truhlar, D. G. Parabolic Tunneling Calculations. *The Journal of Physical Chemistry* **1981**, *85* (6), 624–628.

46. Lamberts, T.; Fedoseev, G.; Kästner, J.; Ioppolo, S.; Linnartz, H. Importance of Tunneling in H-Abstraction Reactions by OH Radicals. *Astronomy & Astrophysics* **2017**, *599*.

47. Kerkeni, B.; Clary, D. C. Quantum Scattering Study of the Abstraction Reactions of H Atoms from CH_3NH_2. *Chemical Physics Letters* **2007**, *438* (1-3), 1–7.

48. Jeong, K. M.; Kaufman, F. Kinetics of the Reaction of Hydroxyl Radical with Methane and with Nine Chlorine- and Fluorine-Substituted Methanes. 1. Experimental Results, Comparisons, and Applications. *The Journal of Physical Chemistry* **1982**, *86* (10), 1808–1815.

APPENDIX A:

REACTANTS

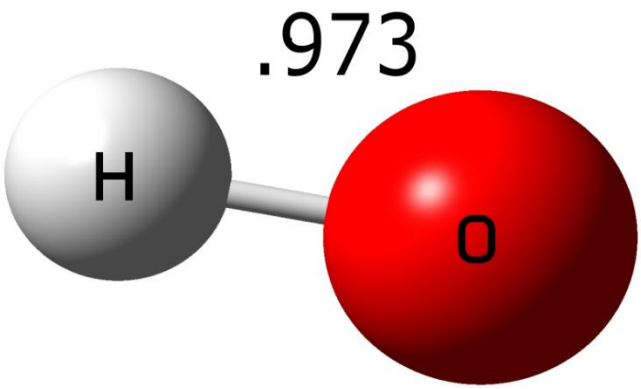

Figure A.2:
Hydroxyl Radical optimized geometry using M06-2X.

Table A.2:

Vibrational modes for hydroxyl radical.

•OH	
Vibrational Mode	Frequency (cm^{-1})
1	3738.68

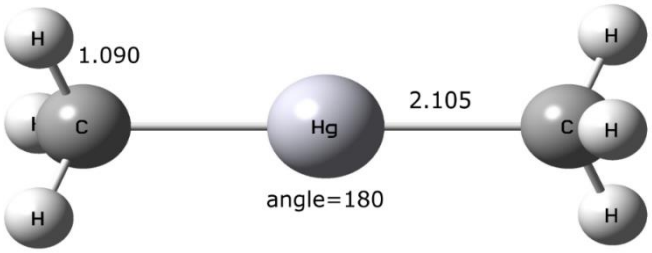

Figure A.1:
Dimethylmercury optimized structure using M06-2X.

Table A.1:

Vibrational modes for Dimethylmercury.

Dimethylmercury	
Vibrational Mode	Frequency (cm^{-1})
1	-71.14
2	147.6
3	151.32
4	514.8
5	531.32
6	691.08
7	699.04
8	777.71
9	784.16
10	1227.64
11	1231.73
12	1465.22
13	1466.46
14	1467.36
15	1468.67
16	3053.65
17	3054.52
18	3138.71
19	3138.77
20	3141.08
21	3141.16

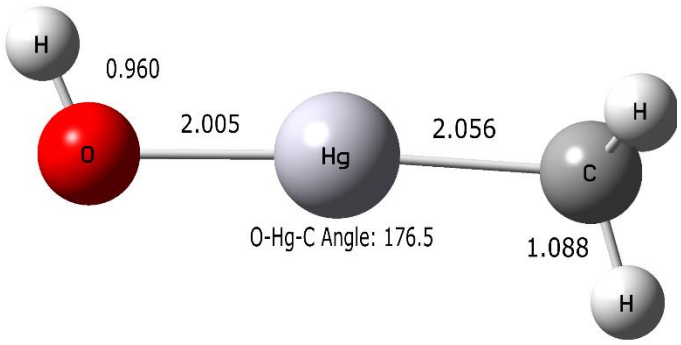

Figure A.3:
Optimized geometry for methylmercury hydroxide using M06-2X.

Table A.3:

Vibrational Modes for methylmercury hydroxide.

MeHgOH	
Vibrational Mode	Frequency (cm^{-1})
1	147.61
2	159.66
3	200.55
4	543.77
5	586.95
6	789.04
7	810.63
8	851.72
9	1258.43
10	1470.73
11	1472.65
12	3069.47
13	3159.71
14	3160.06
15	3913.76

APPENDIX B:

DIMETHYLMERCURY TRANSISTION STATES

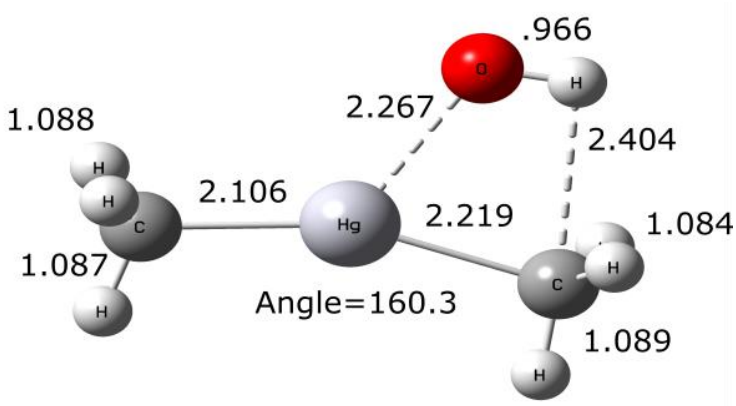

Figure B.1:
Optimized geometry of the transition state for the formation of MeHgOH.

Table B.1:

Vibrational modes for the MeHgOH formation transition state.

MeHgOH formation Transition State			
Vibrational Mode	Frequency (cm^{-1})	Vibrational Mode	Frequency (cm^{-1})
1	-99.77	17	1447.24
2	41.1	18	1465.57
3	126.45	19	1468.83
4	140.69	20	1472.54
5	172.74	21	3072.61
6	217.74	22	3080.95
7	241.94	23	3160.23
8	397	24	3170.94
9	517.13	25	3189.16
10	687.06	26	3219.55
11	693.62	27	3844.08
12	724.72		
13	762.78		
14	773.61		
15	1094.49		
16	1224.93		

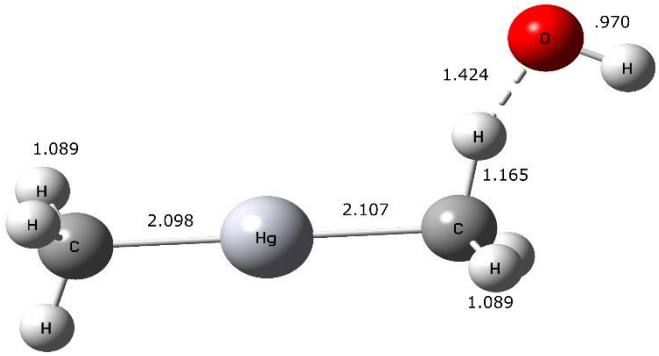

Figure B.2:
Optimized geometry for the hydrogen abstraction channel transition state.

Table B.2:

Vibrational modes for the hydrogen abstraction transition state.

Hydrogen Abstraction

Vibrational Mode	Frequency (cm^{-1})	Vibrational Mode	Frequency (cm^{-1})
1	-637.66	15	1024.39
2	68.04	16	1234.44
3	77.96	17	1294.14
4	144.56	18	1405.04
5	170.13	19	1470.53
6	196.57	20	1471.98
7	296.13	21	1615.34
8	443.25	22	3066.67
9	526.66	23	3108.06
10	604.45	24	3151.89
11	712.29	25	3157.94
12	762.32	26	3179.3
13	792.21	27	3773.45
14	913.3		

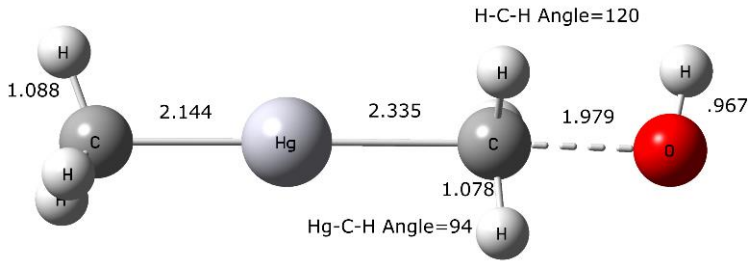

Figure B.3:
Optimized geometry for the MeHg· formation channel transition state.

Table B.3:

Vibrational modes for the MeHg· formation transition state.

MeHg· Formation

Vibrational Mode	Frequency (cm^{-1})	Vibrational Mode	Frequency (cm^{-1})
1	-787.21	15	984.29
2	41.47	16	1180.97
3	74.83	17	1389.11
4	77.39	18	1394.03
5	180.46	19	1457.66
6	202.27	20	1460.41
7	208.79	21	3070.66
8	219.89	22	3111.59
9	473.59	23	3168.56
10	718.13	24	3181.87
11	721.18	25	3279.93
12	825.96	26	3289.57
13	916.12	27	3830.15
14	956.18		

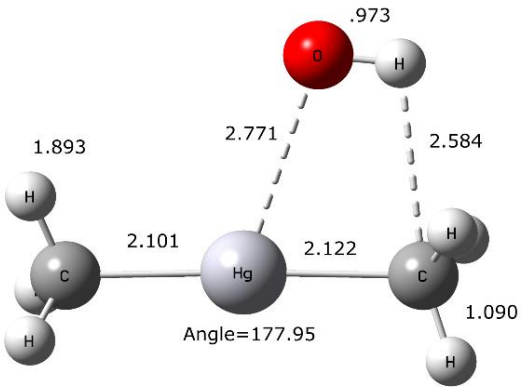

Figure B.4:
Optimized geometry for the pre-reactive complex.

Table B.4:

Vibrational modes for the pre-reactive complex.

Pre-Reactive Complex

Vibrational Mode	Frequency (cm^{-1})	Vibrational Mode	Frequency (cm^{-1})
1	72.24	15	1214.37
2	80.1	16	1231.79
3	107.65	17	1468.05
4	134.19	18	1471.07
5	150.18	19	1473.76
6	180.23	20	1481.31
7	217.55	21	3060.24
8	363.54	22	3062.76
9	503.71	23	3142.52
10	529.47	24	3145.3
11	691.7	25	3151.44
12	705.19	26	3157.83
13	779.65	27	3744.55
14	787.83		

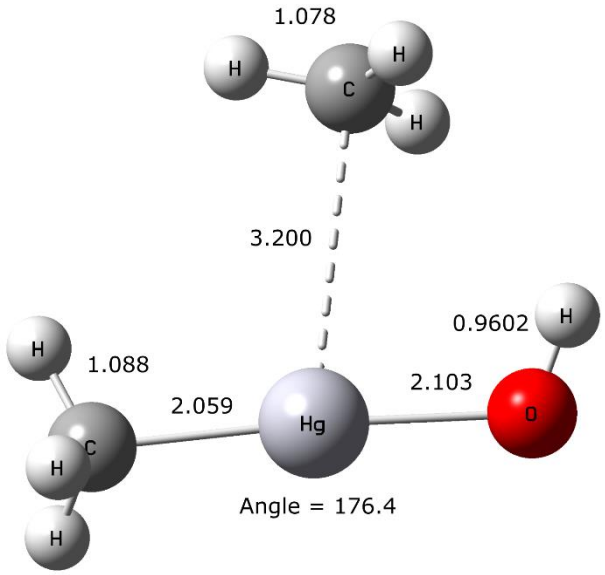

Figure B.5:
Optimized geometry for the post-reactive complex.
Table B.5:

Vibrational modes for the post-reactive complex.

Post-Reactive Complex			
Vibrational Mode	Frequency (cm^{-1})	Vibrational Mode	Frequency (cm^{-1})
1	35.45	15	839.54
2	54.02	16	1255.33
3	86.01	17	1413.43
4	113.47	18	1419.49
5	114.85	19	1475.85
6	166.13	20	1477.93
7	169.87	21	3073.51
8	206.46	22	3130.51
9	254.86	23	3160.13
10	541.04	24	3169.73
11	584.04	25	3306.66
12	586.38	26	3310.98
13	782.95	27	3912.96
14	805.93		

APPENDIX C:

METHYLMERCURY HYDROXIDE TRANSITION STATES

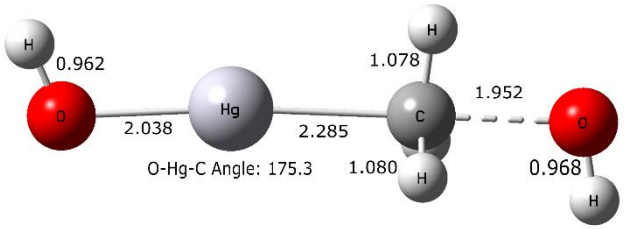

Figure C.1:
Optimized structure for the •HgOH radical formation transition state.

Table C.1:

Vibrational modes for the •HgOH radical formation transition state.

•HgOH Radical Formation

Vibrational Mode	Frequency (cm^{-1})	Vibrational Mode	Frequency (cm^{-1})
1	-906.9	12	965.54
2	61.11	13	1008.64
3	79.73	14	1029.27
4	197.85	15	1394.13
5	202.14	16	1394.61
6	213.37	17	3105.37
7	216.48	18	3270.02
8	229.04	19	3287.34
9	525.46	20	3817.05
10	838.96	21	3876.84
11	857.64		

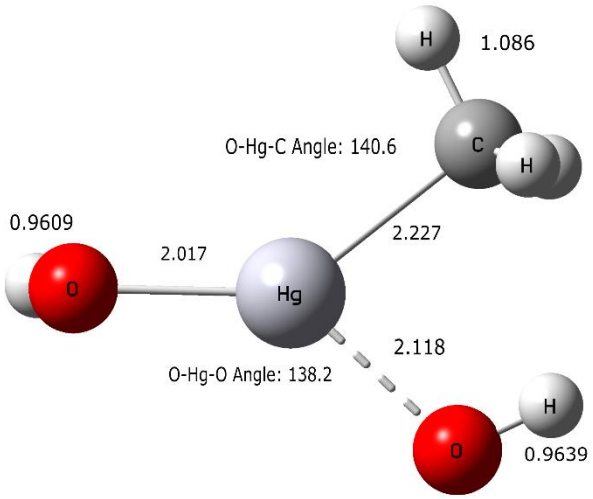

Figure C.2:
Optimized geometry of the $Hg(OH)_2$ formation transition state.

Table C.2:

Vibrational modes of the $Hg(OH)_2$ formation transition state.

$Hg(OH)_2$ Transition State			
Vibrational Mode	Frequency (cm^{-1})	Vibrational Mode	Frequency (cm^{-1})
1	-134.7	12	822.81
2	77.17	13	845.28
3	133.35	14	1090.03
4	173.55	15	1439.51
5	237.66	16	1453.62
6	252.97	17	3088.03
7	303.53	18	3211.73
8	426.53	19	3238.93
9	558.37	20	3862.94
10	694.15	21	3897.48
11	718.14		

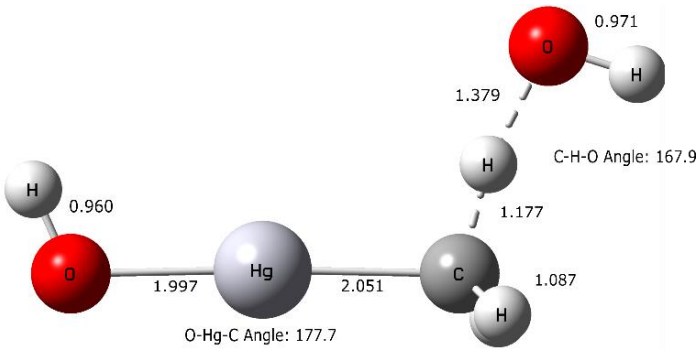

Figure C.3:
Optimized geometry for the hydrogen abstraction (CH_3) transition state.

Table C.3:

Vibrational modes for the hydrogen abstraction (CH_3) transition state.

H-Abstraction Transition State (CH_3)

Vibrational Mode	Frequency (cm^{-1})	Vibrational Mode	Frequency (cm^{-1})
1	-867.24	12	829.86
2	64.52	13	946.1
3	131.3	14	1001.51
4	151.68	15	1273.2
5	168.84	16	1355.53
6	170.65	17	1448.41
7	298.46	18	3115.81
8	495.85	19	3194.11
9	582.53	20	3790.35
10	651.39	21	3910.73
11	809.21		

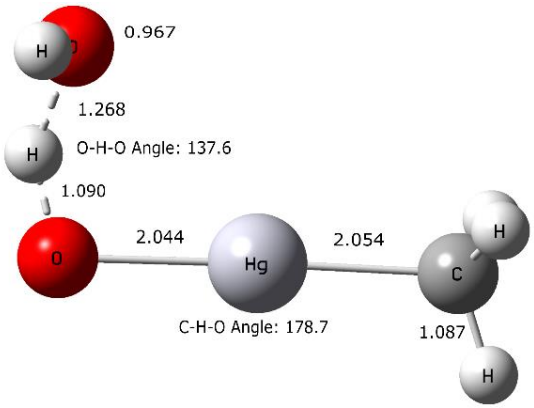

Figure C.4:
Optimized geometries for the hydrogen abstraction (OH) transition state.

Table C.4:

Vibrational modes for the hydrogen abstraction (OH) transition state.

H-Abstraction (OH)

Vibrational Mode	Frequency (cm^{-1})	Vibrational Mode	Frequency (cm^{-1})
1	-1254.99	12	822.1
2	32.27	13	1132.17
3	77.01	14	1259.57
4	144.42	15	1471.4
5	157.42	16	1472.34
6	325.92	17	1816.85
7	488.63	18	3091.3
8	511.59	19	3182.42
9	572.4	20	3184.31
10	706.94	21	3831.7
11	819.67		

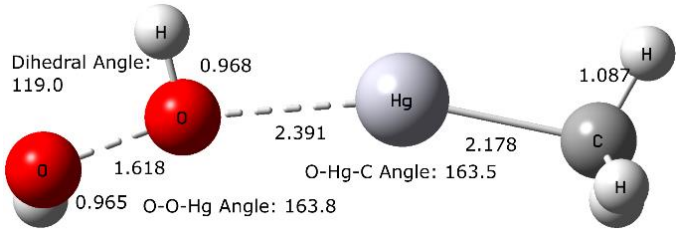

Figure C.5:
Optimized geometry for the •HgMe and peroxide transition state.

Table C.5:

Vibrational modes for the •HgMe and peroxide transition state.

•HgMe + Peroxide Transition State

Vibrational Mode	Frequency (cm^{-1})	Vibrational Mode	Frequency (cm^{-1})
1	-840.5	12	1094.86
2	40.83	13	1141.85
3	54.8	14	1192.13
4	143.27	15	1450.81
5	180.91	16	1458.67
6	205.94	17	3081.57
7	260.76	18	3187.62
8	364.83	19	3202.86
9	426.44	20	3813.91
10	695.95	21	3846.28
11	708.89		

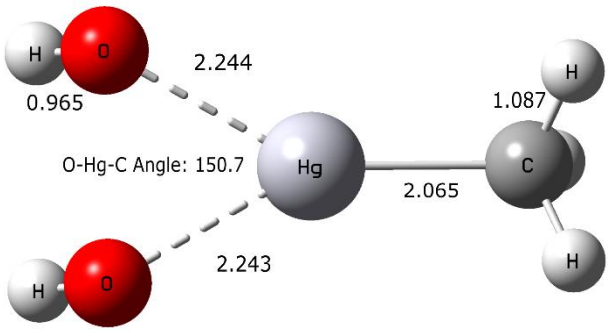

Figure C.6:
Optimized geometry for the MeHgOH reformation transition state.

Table C.6:

Vibrational modes for the MeHgOH reformation transition state.

MeHgOH Reformation Transition State

Vibrational Mode	Frequency (cm^{-1})	Vibrational Mode	Frequency (cm^{-1})
1	-185.53	12	819.64
2	12.56	13	824.48
3	122.87	14	1249
4	136.41	15	1472.29
5	242.37	16	1474.34
6	266.48	17	3097.4
7	383.08	18	3189.47
8	460.07	19	3194.06
9	553.29	20	3852.71
10	613.55	21	3869.28
11	703.73		

APPENDIX D:

PRODUCTS

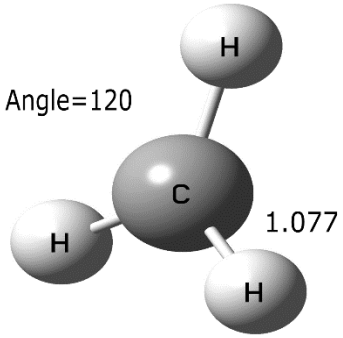

Figure D.1:
Optimized geometry for •CH_3 radical.

Table D.1:

Vibrational modes for •CH_3 radical

•CH_3 radical	
Vibrational Mode	Frequency (cm^{-1})
1	495.63
2	1415.23
3	1415.27
4	3140.53
5	3318.09
6	3318.24

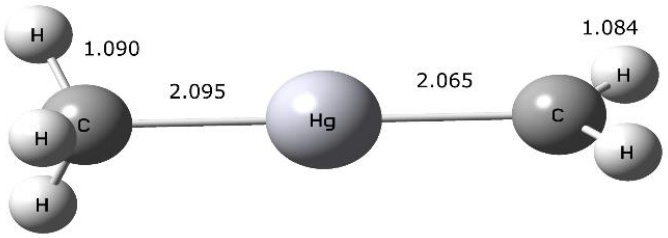

Figure D.2:
Optimized geometry for $MeHgCH_2$· radical.

Table D.2:

Vibrational modes for $MeHgCH_2$· radical.

$MeHgCH_2$·	
Vibrational Mode	Frequency (cm^{-1})
1	113.16
2	157.84
3	159.96
4	500.53
5	530.88
6	553.74
7	662.3
8	760.76
9	777.01
10	1244.09
11	1388.81
12	1468.28
13	1470.9
14	3063.66
15	3146.99
16	3152.89
17	3159.17
18	3258.02

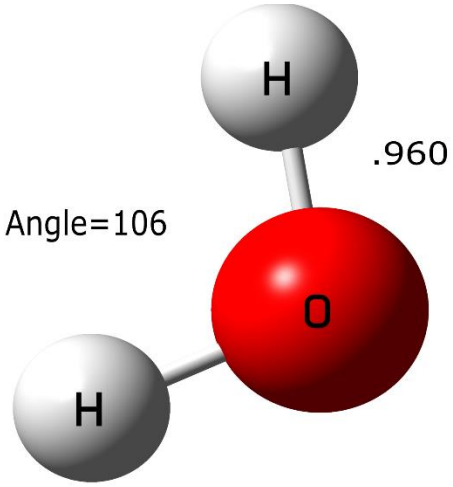

Figure D.3:
Optimized geometry for H_2O.

Table D.3:

Vibrational frequencies for H_2O.

H_2O	
Vibrational Mode	Frequency (cm^{-1})
1	1605.79
2	3868.06
3	3975.41

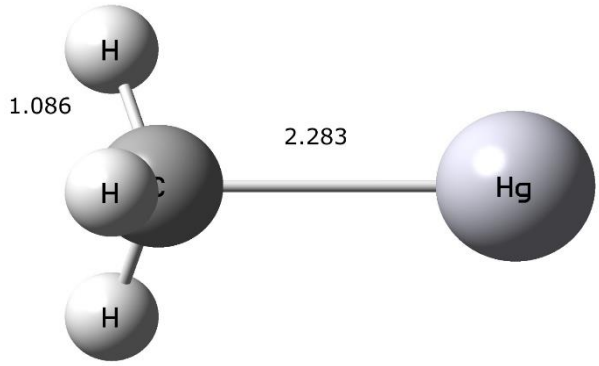

Figure D.4:
Optimized geometry for MeHg• radical.

Table D.4:

Vibrational modes for MeHg• radical

MeHg• Radical	
Vibrational Mode	Frequency (cm^{-1})
1	293.14
2	604.46
3	625.32
4	1043.55
5	1438.52
6	1442.35
7	3075.72
8	3195.89
9	3212.39

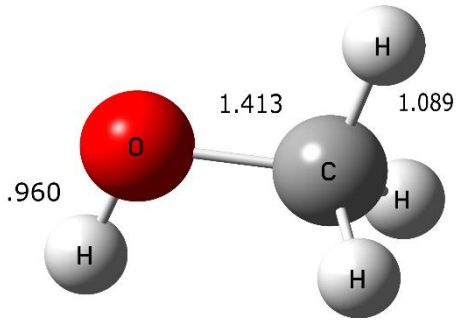

Figure D.5:
Optimized geometry for methanol.

Table D.5:

Vibrational modes for methanol.

Methanol	
Vibrational Mode	Frequency (cm^{-1})
1	373.56
2	1075.57
3	1118.9
4	1183.81
5	1377.83
6	1487.36
7	1502.1
8	1520.65
9	3032.49
10	3090.87
11	3136.64
12	3898.04

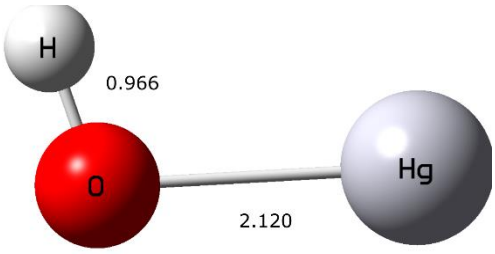

Figure D.6:
Optimized geometry for •HgOH radical.

Table D.6:

Vibrational modes for •HgOH radical.

•HgOH radical	
Vibrational Mode	Frequency (cm^{-1})
1	395.25
2	797.88
3	3832.68

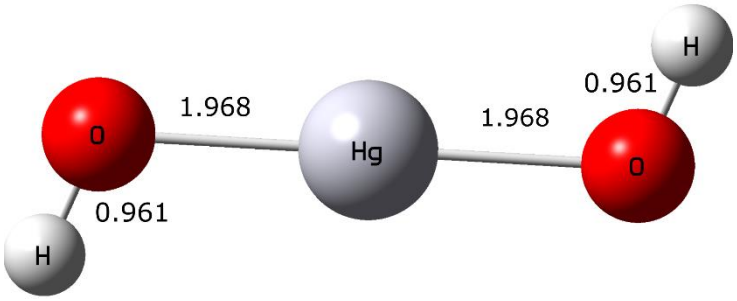

Figure D.7:
Optimized geometry for $Hg(OH)_2$

Table D.7:

Vibrational modes for $Hg(OH)_2$

$Hg(OH)_2$	
Vibrational Mode	Frequency (cm^{-1})
1	151.47
2	170.08
3	212.98
4	580.57
5	635.92
6	915.8
7	945.76
8	3891.32
9	3892.89

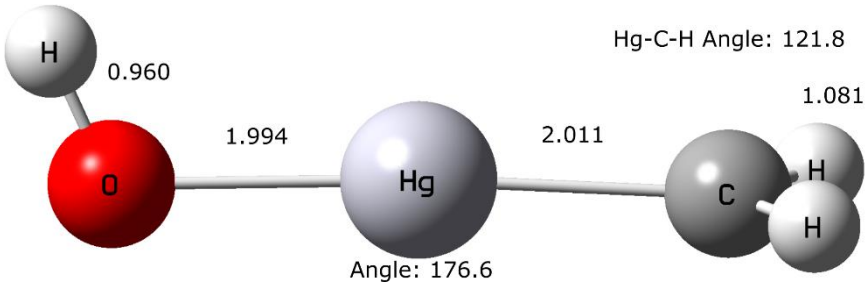

Figure D.8:
Optimized geometry for ·CH_2HgOH radical.

Table D.8:

Vibrational modes for ·CH_2HgOH radical.

·CH_2HgOH Radical	
Vibrational Mode	Frequency (cm^{-1})
1	156.64
2	172.09
3	206.42
4	454.04
5	572.93
6	619.1
7	748.2
8	847.22
9	1388.17
10	3172.55
11	3283.42
12	3913.59

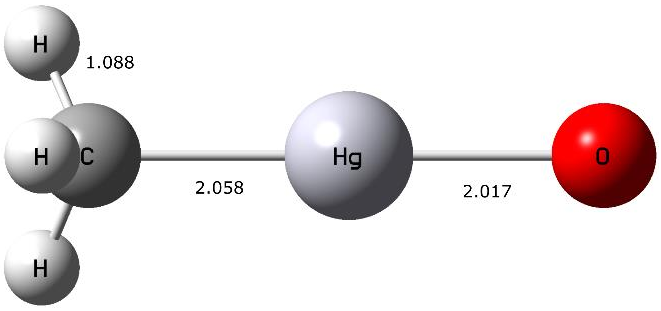

Figure D.9:
Optimized geometry for MeHgO• radical

Table D.9:

Vibrational modes for MeHgO• radical.

MeHgO• Radical	
Vibrational Mode	Frequency (cm^{-1})
1	156.07
2	157.56
3	532.42
4	573.12
5	799.42
6	808.83
7	1255.43
8	1468.12
9	1471.17
10	3070.58
11	3162.89
12	3163.03

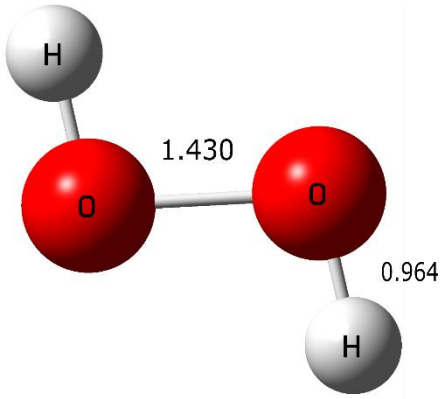

Figure D.10:
Optimized geometry for peroxide.

Table D.10:

Vibrational modes for peroxide.

Peroxide	
Vibrational Mode	Frequency (cm^{-1})
1	-284.9
2	1049.38
3	1265.8
4	1554.53
5	3859.54
6	3868.05